Geoscientific Model Development Discussions

A simulation study of the ensemble-based data assimilation of satellite-borne lidar aerosol observations

T. T. Sekiyama[1], T. Y. Tanaka[1], and T. Miyoshi[2]

[1]Meteorological Research Institute, Tsukuba, Japan
[2]Department of Atmospheric and Oceanic Science, University of Maryland, College Park, Maryland, USA

Correspondence to: T. T. Sekiyama (tsekiyam@mri-jma.go.jp)

GMDD

5, 1877–1947, 2012

OSSEs for satellite lidar observations

T. T. Sekiyama et al.

Title Page

Abstract	Introduction
Conclusions	References
Tables	Figures

|◄ | ►|

◄ | ►

Back | Close

Full Screen / Esc

Printer-friendly Version

Interactive Discussion

Abstract

A four-dimensional ensemble-based data assimilation system was assessed by observing system simulation experiments (OSSEs), in which the CALIPSO satellite was emulated via simulated satellite-borne lidar aerosol observations. Its performance over a three-month period was validated according to the Method for Object-based Diagnostic Evaluation (MODE), using aerosol optical thickness (AOT) distributions in East Asia as the objects of analysis. Consequently, this data assimilation system demonstrated the ability to produce better analyses of sulfate and dust aerosols in comparison to a free-running simulation model. For example, the mean centroid distance (from the truth) over a three-month collection period of aerosol plumes was improved from 2.15 grids (≈ 600 km) to 1.45 grids (≈ 400 km) for sulfate aerosols and from 2.59 grids (≈ 750 km) to 1.14 grids (≈ 330 km) for dust aerosols; the mean area ratio (to the truth) over a three-month collection period of aerosol plumes was improved from 0.49 to 0.76 for sulfate aerosols and from 0.51 to 0.72 for dust aerosols. The satellite-borne lidar data assimilation successfully improved the aerosol plume analysis and the dust emission estimation in the OSSEs. These results present great possibilities for the beneficial use of lidar data, whose distribution is vertically/temporally dense but horizontally sparse, when coupled with a four-dimensional data assimilation system. In addition, sensitivity tests were conducted, and their results indicated that the degree of freedom to control the aerosol variables was probably limited in the data assimilation because the meteorological field in the system was constrained to weather reanalysis using Newtonian relaxation. Further improvements to the aerosol analysis can be performed through the simultaneous assimilation of aerosol observations with meteorological observations. The OSSE results strongly suggest that the use of real CALIPSO data will have a beneficial effect on obtaining more accurate sulfate and dust aerosol analyses. Furthermore, the use of the same OSSE technique will allow us to perform a prior assessment of the next-generation lidar satellite EarthCARE, which will be launched in 2015.

1 Introduction

Atmospheric aerosols from both natural and anthropogenic origins have a considerable influence on weather and climate changes as well as air quality (IPCC, 2007). Thus, in recent years, the study of aerosols has attracted more attention than ever before. However, it is difficult and cost intensive to measure aerosols at the global and synoptic scales, even though further observations are necessary to improve our comprehension of aerosol distributions and properties in the Earth's atmosphere. Given this situation, data assimilation plays an important role in extracting the most out of the available observations. Data assimilation optimally integrates observations and model simulations and maximally exploits the information contained in the observations (cf. Lewis et al., 2006; Park and Xu, 2009; Lahoz et al., 2010). Indeed, several studies have applied data assimilation methods of analyzing aerosols. A simple data assimilation method known as the Optimal Interpolation (OI) was implemented by Collins et al. (2001) for the Advanced Very High Resolution Radiometer (AVHRR) aerosol optical thickness (AOT) observations, by Yu et al. (2003) for Moderate Resolution Imaging Spectro-radiometer (MODIS) AOT observations, and by Tombette et al. (2009) for surface observations of PM_{10}. Because OI can handle only model forecast variables, AOT must be translated into aerosol concentration profiles using many assumptions in their data assimilation systems, resulting in a large analysis error. Another data assimilation method known as the three-dimensional variational data assimilation method (3D-Var) was implemented by Generoso et al. (2007) for the POLarization and Directionality of Earth's Reflectances (POLDER) AOT observations, by Niu et al. (2008) for surface visibility and satellite-measured dust loading observations, and by Zhang et al. (2008) for MODIS AOT observations. The 3D-Var employs an observation operator that properly converts model forecast variables to the AOT. In both OI and 3D-Var, however, the background error covariance is estimated by averaging over a long period of time and represents the climatological mean. This fixed background error covariance is unaware of the flow of the day, e.g. the aerosol plume. Advanced data assimilation methods,

OSSEs for satellite lidar observations

T. T. Sekiyama et al.

four-dimensional variational (4D-Var) or Ensemble Kalman Filter (EnKF), can handle such local disturbances properly through flow-dependent background error covariance. Focusing on only a dust aerosol and using very local observation data, 4D-Var was implemented by Yumimoto et al. (2008) for ground-based lidar dust extinction observa-

5   tions identified from its depolarization ratio, and EnKF was implemented by Lin et al. (2008a,b) for surface observations of PM_{10}. Furthermore, targeting multiple aerosol species and using worldwide aerosol observations, the European Centre for Medium-Range Weather Forecasts (ECMWF) developed a 4D-Var data assimilation system (Benedetti et al., 2009), and Schutgens et al. (2010) developed an EnKF data assimi-

10 lation system. Benedetti et al. (2009) used MODIS AOT observations, and Schutgens et al. (2010) used the ground-based sun-photometer AOT observations of the AErosol RObotic NETwork (AERONET) for their data assimilation systems. AOT is a column-integrated amount; therefore, the disadvantage of using only AOT is that vertical profile information depends only on the model simulation results.

15   The authors of this paper, Sekiyama et al. (2010), developed a four-dimensional EnKF data assimilation system for the Cloud-Aerosol Lidar and Infrared Pathfinder Satellite Observations (CALIPSO)/Cloud-Aerosol Lidar with Orthogonal Polarization (CALIOP) observations. CALIPSO/CALIOP, which is the only satellite-borne aerosol lidar in operation, has a zero viewing angle and a zero swath width; therefore, it cannot

20 obtain horizontally planar images, but it can obtain the cross-section images just below the CALIPSO orbit with an extremely high time/vertical resolution (Winker et al., 2007). Sekiyama et al. (2010) directly assimilated the Level 1B data of CALIPSO/CALIOP, i.e., pre-retrieved satellite observations (attenuated backscatter and its depolariza-tion ratio), and successfully isolated a dust aerosol from the other aerosols. Further-

25 more, Sekiyama et al. (2011b) estimated the Asian Dust emission intensity using the CALIPSO/CALIOP 4D-EnKF data assimilation system. They validated their aerosol analysis through a comparison with independent ground-based lidar observations and operational weather reports in Japan. However, the objective and quantitative verifi-cation of their aerosol analysis has not yet been particularly successful at the global

or synoptic scale most likely because of the insufficient number of aerosol observations independent of the data assimilation. The insufficiency problem includes the uneven distribution of observations. The deployment of ground-based observation sites is sparse and uneven. The observations of MODIS are frequently missed by clouds or high-albedo Earth surfaces. CALIPSO/CALIOP has an extremely narrow viewing angle and is often obstructed from observing the aerosols by clouds. Therefore, the large area comparison between analyses and observations cannot be objectively performed for aerosols, even though such a comparison was successfully performed for weather components: for example, precipitation distribution. The aerosol data assimilation studies described previously were confronted with the same validation problem. Because objective, quantitative, and extensive validation is almost impossible for aerosol data assimilation results, it is difficult to explore the optimal parameter settings of inflation or localization for the EnKF algorithm. It is also difficult to assess the robustness of the EnKF system against a decrease in ensemble members or in the amount of observational information. Among the various aerosol species, only a dust aerosol can be isolated relatively easily during its outbreak because the dust aerosol plume has a high concentration and high depolarization ratio. Consequently, Sekiyama et al. (2010, 2011b) were able to validate their dust aerosol analyses to a limited extent. Other aerosols, however, such as sulfate and smoke, cannot be measured and isolated with high accuracy and high frequency at a global or synoptic scale for model verification. In this situation, observing system simulation experiments (OSSEs) are very useful tools for evaluating the performance of data assimilation systems.

OSSEs have been conducted by various scientists for different purposes (cf. Atlas, 1997; Masutani et al., 2010a,b; Andersson and Masutani, 2010). OSSEs are typically designed to evaluate the potential impacts of prospective observing systems and instruments, such as satellites. The most common motivation for conducting OSSEs is to estimate the cost effectiveness of new observations. In addition, a data assimilation system itself can be tested by OSSEs because of the existence of a known "truth" in the context of OSSEs. The OSSE technique uses a model-generated proxy for the

OSSEs for satellite lidar observations

T. T. Sekiyama et al.

real atmosphere, commonly called the Nature Run. This generation is performed using a realistic atmospheric model in a free-running mode without data assimilation. Simulated observations are generated by virtual instruments from the Nature Run and used as real observations in data assimilation experiments. The generation of these simulated observations includes the addition of realistic errors, which are completely comprehended. In these idealized experiments, the Nature Run provides the "truth" of the atmosphere, which is never obtained from the real atmosphere observations. In OSSEs, all the data assimilation results can be validated against this "truth" without any spatiotemporal maldistribution. Assessment using OSSEs is a well-established technique in numerical weather predictions (NWP), in which objective and quantitative evaluations are provided for data assimilation systems; however, OSSEs require expert knowledge in observation technology, model simulation, and data assimilation (cf. Lahoz et al., 2010). The aim of this study is to assess whether the aerosol data assimilation system (Sekiyama et al. 2010, 2011b) has the ability to produce a better analysis of dust and sulfate aerosols with the use of the OSSE technique. This study is the first OSSE assessment in which satellite-borne lidar observations are simulated, assimilated, and validated, to the best of the authors' knowledge. As demonstrated in the following sections, the OSSE results successfully indicate the beneficial impact of the satellite-borne lidar data assimilation. Furthermore, we explore the optimal parameter settings of inflation and localization for the EnKF algorithm and assess the robustness of the EnKF system against a decrease in ensemble members and the amount of observational information.

Section 2 provides a description of the data assimilation system, which is composed of an ensemble Kalman filter, a global aerosol model, and a lidar observation operator. The experimental design of our OSSE is given in Sect. 3, in which we implement a Nature Run and simulate observation data. An overview of the evaluation tools used in this study is discussed in Sect. 4. The experimental results are presented and discussed in Sect. 5, and the conclusions are presented in Sect. 6.

2   Data assimilation system

The data assimilation system used in this OSSE study is the same version used by Sekiyama et al. (2010, 2011b). CALIPSO Level 1B lidar data (attenuated backscatter and its depolarization ratio) are directly assimilated using the four-dimensional local ensemble transform Kalman filter (4-D LETKF) in this system. A first guess in the data assimilation process is provided by a global aerosol model. Model variables are converted to lidar observables by an observation operator. The details of this data assimilation system are described in the following sections.

2.1   Data assimilation scheme

2.1.1   Ensemble Kalman filter

The Kalman filter is a very powerful tool that produces a statistically optimal estimate of the system state (Kalman, 1960). However, the calculation cost of the Kalman filter is computationally unfeasible for any realistic geophysical models without major simplifications because these models have an enormous state space size. Evensen (1994) suggested that the Kalman filter could be simplified by computing the background error covariance with ensemble forecasts for complicated geophysical systems. This technique, the ensemble Kalman filter (EnKF), has rapidly gained popularity for geophysical data assimilations in recent years because of its simple formulation and implementation in comparison to the 4D-Var. The 4D-Var implementation requires the tangent linear model and the adjoint model of forward simulation models, of which the development and maintenance are heavily labor intensive when handling a strongly nonlinear system, such as the atmosphere. In contrast, the EnKF calculation requires neither tangent linear models nor adjoint models. While 4D-Var and EnKF are the most sophisticated schemes for atmospheric data assimilation in the past decade (Kalnay et al., 2007), the simpler implementation of the EnKF is very beneficial for the data assimilation of atmospheric chemistry because the modeling of the chemical reactions and

emission/diffusion/deposition processes is generally more complicated than weather modeling.

The basic concept of EnKF is that the ensemble of state vectors x_k^b represents the probability density function (PDF) of the system state. Namely, the background error covariance can be estimated as $\mathbf{P}^b = 1/(K-1) \times \mathbf{X}^b(\mathbf{X}^b)^T$, where $\mathbf{X}^b$ is the matrix of which k-th column contains a departure of the k-th ensemble forecast from its ensemble mean $(x_k^b - \bar{x}^b)$, and K is the ensemble size. The matrix $\mathbf{P}^b$ contains the flow-dependent error covariance among the model variables. The EnKF is mathematically equivalent to the original Kalman filter, under the ideal conditions that the simulation model is linear and the EnKF employs an infinite ensemble size. The EnKF produces an analysis using the background error covariance matrix. When the model variables are physically or chemically related to each other, the background error covariance provides information to correct the background errors with observations. Meanwhile, the EnKF is mathematically equivalent to the 4D-Var when the model is linear, ensemble members are infinite, the PDF is Gaussian, and the same background error covariance matrix is used for both (e.g. Bouttier and Courtier, 1999). There is no fundamental discrepancy between the two data assimilation methods, and their differences arise from the non-Gaussianity and nonlinearity of the real atmosphere. Furthermore, as in the 4D-Var or 3D-Var, the EnKF can treat observation operators, which enables the direct assimilation of measured physical quantities not explicitly included in the model forecast variables. The observation operators transform model variables (e.g. temperature) into observable quantities (e.g. satellite-measured radiances). Note that it is possible for an observation operator to include nonlinear processes (e.g. the relationship between aerosol concentrations and attenuated backscattering coefficients). This characteristic is very useful for assimilating the observations of active remote sensors, such as lidars.

In this study, we utilized the local ensemble transform Kalman filter (LETKF), which is one of the EnKF implementation schemes (Hunt et al., 2007). The LETKF uses the ensemble transform approach (Bishop et al., 2001) to obtain the analysis ensemble as

Full Screen / Esc

Printer-friendly Version

Interactive Discussion

a linear combination of the background ensemble forecasts. The LETKF handles observations locally in space, where all the observations are assimilated simultaneously. The EnKF tends to be easily influenced by sampling errors at long distances because the available ensemble size is relatively too small to estimate the background error co-
5 variance of the atmosphere system. Therefore, the covariance localization must be applied for all the EnKF implementation schemes to reduce the spurious impact of distant observations. The LETKF permits a flexible choice of observations to be assimilated at each grid point. The version of the LETKF used in this study employs localization with a Gaussian weighting function that depends on the physical distance between the grid
10 location and the observation (Miyoshi et al., 2007). The limited ensemble size causes both sampling errors at long distances and filter divergence. Moreover, the ensemble forecasts tend to underestimate the background errors in the state estimation because of the limited ensemble size, model imperfections, and nonlinearity. This underestimation leads to filter divergence. To compensate for the error underestimation and avoid
15 the filter divergence, it is necessary to increase the ensemble spread every data assimilation cycle. This technique is called covariance inflation. In this study, we utilized a multiplicative inflation method, in which the ensemble spread is uniformly multiplied by a constant value larger than one. It is common to tune this inflation factor empirically. Furthermore, adding random perturbation to the initial state of each ensemble
20 member is sometimes necessary to maintain the diversity of the ensemble members and not to lose the error covariance among the model variables. In this study, random perturbations were added to several of the variables, as described in Sect. 2.4.

2.1.2 4-dimensional expansion

Hunt et al. (2004) expanded the EnKF four-dimensionally to assimilate observations
25 asynchronously. This expansion allows the EnKF to assimilate observations at the appropriate time and, when available, to use future observations as with the 4D-Var. This expansion was applied to the LETKF in this study (cf. Miyoshi and Aranami, 2006; Kalnay, 2010). The four-dimensional LETKF (4D-LETKF) permits the creation

of a smoother, which is mathematically equivalent to an Ensemble Kalman Smoother (EnKS). The observational increments in the 4D-LETKF are expressed as linear combinations of the forecast perturbations at the time of the observation. This four-dimensional expansion allows the use of the same coefficients to transport the obser-
5 vational increments either forward or backward in time to the analysis time. In other words, under the assumption that the transform matrix is valid at any time within the assimilation time window, the analysis can be obtained by incorporating observations in both past and future times within the time window. The 4D-LETKF determines the linear combination of the ensemble forecasts by estimating the time-independent weights
10 that optimally fit the observations throughout the assimilation time window. Note that although a long time window enables the use of temporally more distant observations, the adverse effect of the model imperfection and nonlinearity becomes more significant at a temporally long distance. Therefore, the 4D-LETKF works only when the assimilation time window is short enough to neglect these model errors and nonlinear-
15 ities. In this study, the analysis is obtained at the intermediate time of the assimilation time window. The analysis of the intermediate time is used to provide the initial conditions of the next ensemble forecast. Temporal localization is applied to this process in the same manner as the spatial localization, with a Gaussian weighting function to reduce the sampling error of the temporally distant observations. Figure 1 illustrates
20 the schematic diagram of the 4D-LETKF data assimilation cycle. In this case, the time window is 48 h long, and the analysis is updated at 24-h intervals. Each observation is used twice with normalizing weights. This 4D-LETKF implementation is identical to that of Miyazaki et al. (2011), and similar to the "Running in Place" algorithm proposed by Kalnay (2010) and Yang et al. (2012), in which the spin-ups are rapidly performed for
25 suddenly evolving phenomena by recycling the observations repeatedly. Kalnay (2010) proposed a severe storm as an example of a suddenly evolving phenomenon. Likewise, aerosol outbreaks also develop rapidly. This 4D-LETKF module was successfully applied to ozone data assimilation by Sekiyama et al. (2011a).

OSSEs for satellite lidar observations

T. T. Sekiyama et al.

Full Screen / Esc

Printer-friendly Version

Interactive Discussion

2.1.3 State vector augmentation

To acquire the inverse analysis of dust emission intensity from atmospheric observations, we introduce the dust emission factor optimally estimated by the 4D-LETKF. Generally, in aerosol simulation models, the dust emission flux F_{ij} is calculated at each
5 land surface grid (i, j) as follows:

$$F_{ij} = A_{ij} f(u^*_{ij}), \tag{1}$$

where A_{ij} is the function of ground surface conditions (e.g. soil moisture content, snow cover ratio, vegetation cover ratio, land-use type, and soil type) that ranges between 0
10 and 1, and f is the dust emission flux estimated by a wind erosion model as a function of a surface friction velocity u^*. In this study, the dust emission flux F_{ij} is corrected by the dust emission factor α_{ij} as follows:

$$F'_{ij} = \alpha_{ij} F_{ij}. \tag{2}$$

15 The dust emission factor α_{ij} is estimated at each land surface grid (i, j) by the data assimilation. Here, we use an augmented state vector $\boldsymbol{x}'$ consisting of both the atmospheric state variables at all model surface grid points and the dust emission factor at all model surface grid points as follows:

$$\boldsymbol{x}' = (\boldsymbol{x}^\mathsf{T}, \boldsymbol{\alpha}^\mathsf{T})^\mathsf{T}, \tag{3}$$

20

where $\boldsymbol{x}$ is the state vector that consists of the model state variables, $\boldsymbol{\alpha}$ is the parameter vector that consists of all the dust emission factors α_{ij}, and T denotes transposition. The augmented state vector $\boldsymbol{x}'$ is then used for the data assimilation processes instead of the original state vector $\boldsymbol{x}$. This augmentation enables the 4D-LETKF to estimate the
25 parameters, such as dust emission factors, through the background error covariance with the model state variables (cf. Kang et al., 2011; Miyazaki et al., 2011; they studied CO_2 flux estimation). In other words, the state vector augmentation method simultaneously estimates the aerosol concentrations (i.e., state variables) together with the

surface emission intensity (i.e., unknown parameters). Therefore, it is essential to this inverse analysis to successfully estimate the background error covariance between the dust concentrations and dust emissions. Figure 2 presents the spatial correlation between surface dust concentrations and the dust emission within the square area centered at (43° N, 112.5° E), which is equivalent to the background error covariance distribution. This spatial distribution indicates the response pattern of the dust concentrations as an increase in the dust emission within the square area. These correlations were derived from the result of a 32-member ensemble 24-h forecast using the same aerosol model as that used in the data assimilation system. High positive correlation areas are evidently located in the downwind directions from the emission area. Such an informative distribution is necessary for a successful inverse analysis.

In this formulation, aerosol models do not forecast the dust emission factors; therefore, the factors are constant during forward forecasting. In other words, we assume a persistent forecast model ($M = I$, when $\alpha_n = M\alpha_{n-1}$; I denotes an identity matrix, and n means the time step) for the dust emission factors because of the lack of any application for the forecast model. This is a typical approach to parameter estimation, but it is a very simplified assumption; therefore, the error information of the dust emission is not propagated during forward forecasting. Consequently, unless the covariance magnitudes related to these parameters are inflated, the ensemble spread cannot remain meaningful and be influenced by the observations. In this case, the estimation of the surface dust emission will diverge. Thus, in this study, the ensemble members of the dust emission intensity are perturbed by adding a random Gaussian noise, simultaneously with the multiplicative inflation of the background error covariance.

2.2 Global aerosol model

In this study, we applied the 4D-LETKF to an aerosol chemistry-transport model, the Model of Aerosol Species in the Global Atmosphere (MASINGAR), which was developed by the Meteorological Research Institute (MRI) of Japan (Tanaka et al., 2003; Tanaka and Chiba, 2005). MASINGAR has a dynamical meteorological component

Back | Close

Full Screen / Esc

Printer-friendly Version

Interactive Discussion

Printer-friendly Version

Interactive Discussion

with chemical processes; its prognostic variables are horizontal winds, temperature, humidity, and surface pressure. The version of MASINGAR for the OSSE has a horizontal resolution of approximately $2.8° \times 2.8°$ (T42 spectrum truncation) and 30 vertical layers in a hybrid sigma-pressure coordinate from the Earth's surface to the stratopause (approximately 7 layers below 800 hPa and 15 layers above 150 hPa). MASINGAR has been successfully used for aerosol studies (Tanaka et al., 2005, 2007, 2011; Tanaka and Chiba, 2006; Uno et al., 2006). MASINGAR includes the emission, advection, diffusion, gravitational settling, wet/dry deposition, and chemical processes of SO_2, dimethyl sulfide (DMS), sulfate aerosol, dust aerosol (partitioned into 10 size bins), organic carbon (OC) aerosol, black carbon (BC) aerosol, and sea-salt aerosol (partitioned into 10 size bins) with an external mixture formation. The sizes and densities of these aerosol particles are presented in Table 1. Volume mean diameters are shown for each dust aerosol size bin. Generally, dust emission flux has a threshold friction velocity, which means that no dust emission occurs when the friction velocity (or wind speed) is lower than a certain value. The threshold friction velocity depends on the dust particle size and soil moisture in MASINGAR. The formulation of Shao and Lu (2000) is adopted to calculate the threshold friction velocity. The vertical flux of dust particles is assumed to be proportional to the saltation flux of soil particles in MASINGAR. The saltation flux is calculated using a formula from Owen (1964), in which the saltation flux depends on the soil particle size, the gravitational settling velocity, the threshold friction velocity, and the smooth friction velocity. We adopted the Special Report on Emissions Scenarios (SRES: Nakicenovic and Swart, 2000) A1 for the anthropogenic SO_2 emission in MASINGAR. The SRES were published by the Intergovernmental Panel on Climate Change (IPCC), in which A1 scenarios were described as a more integrated world with rapid economic growth.

The meteorological field in MASINGAR is nudged to a 6-h interval reanalysis of the Japan Meteorological Agency (JMA) using a Newtonian relaxation scheme, in which dynamic tendencies are added with an 18-h relaxation time constant at each time step to reproduce the realistic meteorological conditions of the global atmosphere. More

details of MASINGAR are described in Tanaka et al. (2003) and Tanaka and Chiba (2005). In this study, all the data assimilation experiments were initiated at 00:00 UTC on 1 March 2007 and terminated at 00:00 UTC on 1 June 2007. The initial condition at 00:00 UTC on 1 March was prepared by a 1-yr simulation performed by MASINGAR without using any aerosol assimilation as a spin-up.

2.3 Lidar observation operator

Similarly to other EnKF schemes and variational schemes, the LETKF can employ an observation operator to directly assimilate the observables not included in the model variables. The observation operator is also used to make simulated observations for OSSEs. This study validates the data assimilation performance of satellite-borne lidar data for the purpose of developing an observation operator to simulate CALIPSO/CALIOP, the only satellite-borne lidar that provides aerosol observations in operation. The observation operator H can be expressed as a sequence of several distinct functions acting on the model state vector $\boldsymbol{x}$,

$$H(\boldsymbol{x}) = G(D(P(\boldsymbol{x}))) \tag{4}$$

where P denotes an interpolation from the grid points to the observation locations; D denotes the physical or chemical relationship relating the aerosol concentration and properties to optical extinction and backscatter; G denotes a possible spatial integration of values, such as attenuated backscatter along the laser beam. CALIPSO/CALIOP provides vertical profiles of the total attenuated backscattering coefficient $\beta'_\lambda(\zeta)$ at 532 and 1064 nm and the volume depolarization ratio ($\delta = \beta'_\lambda(\zeta)_{\text{perpendicular}} / \beta'_\lambda(\zeta)_{\text{parallel}}$) at 532 nm. The attenuated backscattering coefficient $\beta'_\lambda(\zeta)$ at wavelength λ is expressed as follows:

$$\beta'_\lambda(\zeta) = \zeta^2 P_\lambda(\zeta)/C_\lambda = (\beta_{\lambda,\text{m}}(\zeta) + \beta_{\lambda,\text{p}}(\zeta)) T^2_{\lambda,\text{m}}(\zeta) T^2_{\lambda,\text{p}}(\zeta), \tag{5}$$

where $P_\lambda(\zeta)$ is the raw signal intensity from altitude ζ, and C_λ is the instrument constant. Backscattering coefficients are represented by $\beta(\zeta)$, and the two-way transmittance

OSSEs for satellite lidar observations

T. T. Sekiyama et al.

due to scattering (or absorbing) species is given by $T^2(\zeta)$; the subscripts m and p specify the molecular and particulate (either aerosol or cloud) contributions to the signal, respectively. In this study, we assimilated the total attenuated backscattering coefficient $\beta'_\lambda(\zeta)$ and its depolarization ratio $\delta(\zeta)$. This direct assimilation avoids errors due

5 to data retrieval processes. Extinction coefficients and optical thickness, which have generally been used for aerosol assimilation studies, require erroneous assumptions or prior estimations to be retrieved from attenuated backscatter data.

The observational operator simulates atmospheric optics induced by molecules (Rayleigh scattering) and aerosol particles (Mie scattering) at each wavelength λ.

10 $\beta_{\lambda,\mathrm{m}}(\zeta)$ is the backscattering coefficient of the atmospheric molecules, of which the concentrations can be estimated from the model pressure and temperature using the gas law. The transmittance $T_{\lambda,\mathrm{m}}(\zeta)$ can be estimated through the accumulation of the extinction coefficients of atmospheric molecules between the lidar instrument and altitude ζ. The backscattering coefficient of aerosol particles $\beta_{\lambda,\mathrm{p}}(\zeta)$ is the sum of the

15 backscattering coefficients of sulfate, OC, BC, sea-salt, and dust aerosols, of which the concentrations are model prognostic variables. These backscattering coefficients are calculated depending on the aerosol type and size and using the equations of the Mie scattering theory. The transmittance of aerosol particles $T_{\lambda,\mathrm{p}}(\zeta)$ can be estimated through the accumulation of all the extinction coefficients of aerosol particles,

20 as demonstrated for the estimation of $T_{\lambda,\mathrm{m}}(\zeta)$. Table 2 tabulates complex indices of refraction for each aerosol species used in this observation operator. The dust extinction coefficient is empirically approximated using the Mie scattering theory, and the dust backscattering coefficient is estimated using the extinction coefficient divided by an empirical value of 50 sr. It is assumed that only dust particles are nonspherical in this

25 study; hence, depolarization is induced only by dust aerosol. In according with Shimizu et al. (2004), the depolarization ratio δ is set to 0.35, which is optimal for Asian Dust. The coefficients $\beta_{\lambda,\mathrm{p}}(\zeta)$ and $T_{\lambda,\mathrm{p}}(\zeta)$ vary with ambient moisture because the particles have been observed to increase in size according to water uptake. The hygroscopic

growth of the particles is parameterized with relative humidity according to Chin et al. (2002), as shown in Table 3. Dust aerosol is assumed to be completely hydrophobic.

In this study, only sulfate and dust aerosols are included in the control variables. Therefore, the concentrations of OC, BC, and sea-salt aerosols are used only in the observation operator as constrained conditions when the atmospheric optics is simulated. This observation operator is nonlinear, but it requires only forward calculation. EnKFs have a distinct advantage over 3D-Var or 4D-Var in that they do not require a linearized observation operator or its adjoint.

2.4 Experimental conditions

In this data assimilation study, we set the sulfate aerosol concentration, the dust aerosol concentration, and the dust emission factor as the control variables and parameters. These control variables and parameters were updated by the 4D-LETKF every 24 h. Correlations among the observation errors were neglected; namely, the observation error covariance R is a diagonal matrix, which permits a large reduction in computational cost when calculating its inverse matrix. The standard experiment was conducted using 32 ensemble members. Miyoshi and Yamane (2007) noted that the LETKF worked with at least 20 ensemble members for a state-of-the-art atmospheric general circulation model. The sensitivity to the ensemble size was also tested in this study. The localization scale of the Gaussian weighting function was set horizontally to 3000 km, vertically to 10 layers, and temporally to 24 h. The influence of sampling errors on a grid point becomes almost negligible at the distance of these localization scales for all observations. The assimilation time window was 48 h long with a 1-h resolution, and the analysis was performed with the past 24-h and future 24-h observations, as shown in Fig. 1. With the 6000-km horizontal extent and the 48-h time window, it was assumed that almost every aerosol plume was properly detected more than once by the CALIPSO/CALIOP, as long as the sky was clear. The vertical 10-grid length was based on the number of layers in the modeled troposphere. While the use of more observations is preferable, horizontally and temporally distant observations raise the sampling

⏮ | ⏭

◀ | ▶

Back | Close

Full Screen / Esc

Printer-friendly Version

Interactive Discussion

error and the nonlinearity error. Sensitivity to the horizontal localization was also tested in this study. The multiplicative covariance inflation parameter was fixed at 20 % for the standard experiment, and sensitivity to the inflation parameter was tested.

The initial ensemble spreads were generated by adding random Gaussian noise to the initial field. The analysis ensemble in every assimilation cycle was perturbed with zero-mean random Gaussian noise, similarly to additive inflation. The deviations of these additive perturbations were set to $1.0\,\mathrm{m\,s^{-1}}$ for horizontal winds, $1.0 \times 10^{-9}\,\mathrm{kg\,kg^{-1}}$ for the dust concentration, $10\,\mathrm{pptv}$ for the sulfate concentration, and 0.5 for dust emission factors. The purpose of these additive perturbations is to maintain the covariance magnitudes and increase the chances that the ensemble forecasting will explore directions of error growth missed by unperturbed ensembles and avoid being trapped in the unlikely subspace of the chaotic atmosphere system. The corrected dust emission flux F'_{ij} in Eq. (2) was limited to between 0 and 125 % of the maximum emission intensity under the conditions of the no-snow, no-vegetation, and completely dry surface at each grid point (i, j), following the procedure of Sekiyama et al. (2011). This limitation prevents negative emission and overlarge emission. These experimental conditions were empirically chosen to obtain the best performance for East Asia. The optimal experimental conditions depend on the target regions and aerosol species.

In addition to the standard experiment, we conducted several sensitivity-test experiments, as shown in Table 4. The ensemble size test consists of 4 experiments of varying ensemble sizes: 128, 64, 16, and 8 members. The covariance inflation test consists of 3 experiments whose covariance inflations are 5 %, 10 %, and 40 %. The localization scale test has only one experiment, with a horizontal scale of 1000 km. The observation error test consists of 2 experiments whose observation errors are set to 40 % (two-fold larger than the standard setting) and 100 % (five-fold larger than the standard setting). The data density test has two types of experiments: one is a cloudiness test (3 experiments), and the other is a threshold test (1 experiment). The details of the cloudiness and threshold tests are described in Sect. 3.3. We conducted another experiment to explore the impact of the number of satellites on dust emission

estimations, in which four virtual CALIPSOs were available for the data assimilation, as described in Sect. 5.1.2.

3 OSSE design

The preparations for the Observing System Simulation Experiments (OSSEs) are described in this section. These data assimilation experiments spanned the entire globe using a global model and global satellite observations. However, the validation of these experiments was concentrated on only the region of Asia in this study. The highest concentrations of sulfate aerosols have frequently been reported from Asia (WHO Regional Office for Europe, 2006). This region also experiences relatively high dust concentrations (United Nations Environment Programme, 2008). Therefore, the validation of this method in Asia suits the first step of the OSSE aerosol study. The optimal experimental conditions were empirically chosen for East Asia in this study. Furthermore, because the aerosol distributions vary widely between regions, adopting a global mean is inappropriate. The exploration of other regions in addition to East Asia will be a part of our future work.

3.1 CALIOP/CALIPSO

Satellite measurements are extremely powerful at capturing global aerosol distributions at fine temporal and large spatial scales. The purpose of this study is to conduct the OSSE of the CALIPSO/CALIOP and, consequently, to assess the satellite-borne lidar data assimilation. CALIPSO was launched on 28 April 2006 as part of the NASA A-train (cf. Winker et al., 2007). All satellites of the A-train are in a 705-km sun-synchronous polar orbit between 82° N and 82° S with a 16-day repeat cycle, which is an approximately 1000-km longitudinal interval per day at mid-latitudes. An example of one-day CALIPSO orbit tracks is presented in Fig. 3. The primary instrument CALIOP, carried by CALIPSO, was the first satellite polarization lidar to be optimized for both aerosol

and cloud measurements. During both day and night, the CALIOP continuously provides vertical profiles of the total attenuated backscattering coefficient $\beta'_\lambda(\zeta)$ at 532 and 1064 nm and the volume depolarization ratio $\delta(\zeta)$ at 532 nm, with a horizontal resolution between 333 m and 1 km and a vertical resolution of 30–60 m in the troposphere. The CALIOP has a zero viewing angle and a zero swath width; therefore, it cannot obtain horizontally extended planar images, and only the cross-section images directly below the CALIPSO orbit are available with an extremely high resolutions. The values of $\beta'_\lambda(\zeta)$ and $\delta(\zeta)$ are contained in CALIPSO Level 1B datasets with their time references and geo-locations. Winker et al. (2007) indicated that the measurement uncertainties of the CALIOP are approximately 20 %. The CALIPSO science team provides Level 2 data, including the variables retrieved from Level 1B data. The Level 2 data contain Cloud-Aerosol Discrimination (CAD) scores (Liu et al., 2004) with a 5-km horizontal resolution. The CAD score is an indicator that enables the discrimination of target signals between aerosols and clouds. Data assimilation must then identify the aerosol signals, but it is difficult to screen out the cloud signals using model cloud simulations. The CAD score is not a perfect indicator, but it is useful for data screening without model cloud simulations (Sekiyama et al., 2010).

3.2 Making a nature run

A Nature Run, which serves as the truth for OSSEs, is generated by a realistic atmospheric model in a free-running mode without data assimilation. When conducting OSSEs, the Nature Run is the "real" atmosphere. If a process is not included in the atmospheric model, the process does not exist in the computer-generated world. If a mass balance (e.g. the SO_2-SO_4 ratio) exists in the atmospheric model, the mass balance is true in the computer-generated world. In this idealized situation, the Nature Run provides the "truth" of the atmosphere; all the data assimilation results can be validated against this "truth" without any errors. The Nature Run is both the correct answer for analysis validation and the source of simulated observations. Therefore, the Nature Run model results should be realistic and slightly different from the data assimilation

Full Screen / Esc

Printer-friendly Version

Interactive Discussion

T. T. Sekiyama et al.

Discussion Paper | Discussion Paper | Discussion Paper | Discussion Paper

system model results. In this study, we produced the Nature Run by using MASINGAR with slightly different configurations than the MASINGAR installed in the 4D-LETKF data assimilation system. If the model and its configurations are identical for the Nature Run and the data assimilation system, the system is referred to as an identical twin
5 OSSE (Liu and Kalnay, 2007). On the other hand, if the Nature Run model differs from the data assimilation system model, the experiment is referred to as a fraternal twin OSSE (Masutani et al., 2010a). Our OSSEs are categorized as fraternal twin OSSEs.

Because MASINGAR is strongly constrained by the meteorological reanalysis with Newtonian relaxation nudging in this study, its simulation results are less likely to be
10 influenced by the initial conditions. Consequently, to obtain a slightly different meteorological field, we altered the Newtonian relaxation time constant from 18 h to 54 h. In addition, we changed the formulation schemes of dust threshold friction velocity (from Shao and Lu, 2000, to those of Greeley and Iversen, 1985) and changed the saltation flux intensity (from Owen, 1964, to White, 1979) to make a difference in the dust
15 emission. Furthermore, SO_2 and DMS emissions were doubled and then multiplied by a random Gaussian noise with a mean of 1 and a standard deviation of 1 to make a difference in the sulfate aerosol distribution. Figures 4 and 5 show snapshot examples of the difference between the default MASINGAR result and the Nature Run MASINGAR result. The difference is very large in several regions (on the other hands, very small
20 in several regions) for both sulfate and dust aerosol optical thickness (AOT). Generally speaking, the accuracy of aerosol models is much inferior to that of weather forecast models in the real world. It is often the case that the modeled aerosol concentrations are twice or three times larger (smaller) than those of the observed concentrations; it is not uncommon for the difference to reach 10 or 100 times. Therefore, the differences
25 shown in Figs. 4 and 5 appear natural: they are the differences between the model and the truth.

In this study, the Nature Run is the last 3-month period of a 6-month nudged simulation using the Nature Run MASINGAR with the same resolutions and configurations as the default MASINGAR used in the data assimilation system, with the exception of their

Newtonian relaxation time constant, dust flux formulations, and sulfur emissions. The output was saved every hour. The initial condition of the 6-month nudged simulation is the result of a 1-yr free model simulation of the default MASINGAR at 00:00 UTC on 1 December 2006. The Nature Run begins at 00:00 UTC on 1 March 2007 and ends at 00:00 UTC on 1 June 2007. The period from 1 December 2006 to 28 February 2007 was used as a spin-up. A primary reason for selecting this period is that the spring is the season of Asian Dust, and the dust outbreak events were frequently reported during the spring of 2007.

3.3 Making the simulated observation data

In OSSEs, simulated observations are generated by virtual instruments from the Nature Run. These simulated observations are assimilated as if they were real ones measured in the real atmosphere. The virtual instruments of satellite-borne lidars require the simulation of radiances involving many procedures, including the simulation of orbits, the evaluation of cloudiness, and the vertical distributions of aerosols. This simulation can basically be performed by the lidar observation operator (cf. Eq. 4) developed for the 4D-LETKF computation. In addition, these simulated observations must include realistic observation errors that are completely comprehended in contrast to the real observations. The observables we should simulate are the total attenuated backscattering coefficients at 532 and 1064 nm and the volume depolarization ratios at 532 nm, which are included in the CALIPSO/CALIOP Level 1B dataset. These simulated observations are assumed to be observed from the real CALIPSO satellite orbits on the same days of the OSSE period. The transformation from the model grid points to the observation locations (P in Eq. 4) was performed by horizontally interpolating the variables at the four closest grid points of the Nature Run atmosphere onto the observation location and then vertically onto the observation measurement level, in which the vertical interpolation was linear in log pressure.

The emulation of lidar instruments requires a realistic cloud distribution because clouds interfere with the lidar beam reaching the aerosols at similar and lower altitudes.

[Printer-friendly Version](#)

[Interactive Discussion](#)

Hence, cloud evaluation is extremely important in the simulation of lidar observations. The cloud distribution of the Nature Run will significantly affect the sampling of the simulated observation data. Figure 6 depicts a daily-mean cloud distribution of the Nature Run that illustrates the 16-layer sum (varying from 0 to 16) of the cloud cover
5 ratios (varying from 0 to 1) within the troposphere to browse the column amount of the clouds. According to Shibata et al. (1999), the meteorological modules of MASINGAR were well evaluated, and the cloud distribution shown in Fig. 6 appears natural in comparison with the real cloud snapshot taken by the infrared channels of the geostationary meteorological satellite MTSAT-1R located at 140° E on the same day. When fractional
10 cloudiness (= cloud cover ratio) is diagnosed in the model layers, cloud overlap assumptions must be applied to estimate the probability of lidar measurements at each layer. In this study, the cloud fraction was approximated by the random cloud overlap assumption, as follows:

$$C(k) = 1 - {}_n\prod_{i=k}(1 - c_i), \tag{6}$$

15

where $C(k)$ is the cloud fraction over the sky at the model layer k; n is the top layer in the model atmosphere; and c_i is the cloud cover ratio of the model layer i. The missing data rate of layer k was proportionate to $C(k)$. Indeed, maximum-random overlap (i.e., the maximum overlap of adjacent and the random overlap of separate cloud layers)
20 may be a more realistic assumption (e.g. Raisanen, 1998) than the random overlap assumption, but at least the random overlap assumption of Eq. (6) will never underestimate the amount of missing lidar observations due to the existence of clouds. The overestimation of observation availability should be avoided to avoid the overestimation of the data assimilation accuracy. Figure 7 shows the distributions of one-day lidar
25 aerosol observations derived from the real CALIOP and the OSSE virtual lidar with the standard settings. It is notable that these observations were previously screened by the CAD scores or the aerosol signal threshold mentioned in the next paragraph, and the total data amount of CALIOP is larger than that of OSSE virtual lidar because the CALIOP vertical resolution is higher than the Nature Run resolution. However, Fig. 7

enables us to browse the characteristics of the distributions of lidar data that is missing due to clouds. The OSSE virtual lidar tends to be more highly influenced by clouds in the Arctic and the Tropics than the real CALIOP and thus to miss observations in those areas. The sensitivity of the data assimilation performance to the cloud fraction was tested in this study.

In the real CALIPSO/CALIOP data assimilation experiments (Sekiyama et al., 2010), lidar observations were selected only when the aerosol signal was detected according to the CAD score. The selected measurements were then horizontally and vertically averaged along each satellite orbit to approximately model resolution prior to the data assimilation. Such a combined observation is referred to as a "super-observation" (Lorenc, 1981) in data assimilation studies. The use of super-observations reduces both the random errors of individual measurements and the representativeness errors of high-resolution measurements. After the selection and averaging, the total number of the observations to be assimilated was 15 000–25 000 points per day in the global troposphere. In this OSSE study, instead of using the CAD score, we defined the threshold of the aerosol signal above which the simulated observations are used in the data assimilation. The 532-nm extinction coefficient, which was computed by the observation operator, was used as the aerosol signal proxy, and the threshold was set to $2 \times 10^{-5}\,\mathrm{m}^{-1}$. After the cloud-cover and threshold data screening, the total number of the simulated observations to be assimilated was 10 000–20 000 points per day in the global troposphere. The sensitivity of the data assimilation performance to this threshold was tested in this study. The frequency distributions of the selected observations to be assimilated are shown in Fig. 8. This comparison provides information on the plausibility of the simulated observations. Although the simulated data amounts are less than the real ones because these observations are not yet vertically averaged to the model resolution (the CALIOP vertical resolution is higher than the Nature Run resolution), the shapes of the frequency distributions are analogous with each other.

Finally, the simulated observations were produced by adding simulated observation errors, which roughly correspond to the type of random errors found in the real

observations. If the simulated observation errors are too small, the OSSEs will result in presenting an unrealistic benefit of the simulated observations. Winker et al. (2007) indicate that the measurement uncertainties of CALIOP are approximately 20 %, although it is impossible to separate instrument errors from representativeness errors and estimate the minimum error. We assumed that the observation errors were unbiased and, consequently, added a zero-mean random Gaussian noise to each observation with a 20 % standard deviation of each observation value. To avoid a too-small error, the minimum observation error was set to $1 \times 10^{-4} \, \mathrm{sr}^{-1} \, \mathrm{km}^{-1}$ for both 532 and 1064 nm. The observation error of the depolarization ratio was calculated from multiplying a parallel component error and a perpendicular component error together. The sensitivity of the data assimilation performance in comparison to the simulated observation error was tested in this study. An example of the cross sections, in which both the real and simulated lidar observations $\beta'_{\lambda=532}(\zeta)$ are plotted, is shown in Fig. 9. The simulated observations have vertically discrete layers depending on the model resolution, distributing them into strips. The two cross sections illustrate the same day and location, but unfortunately, their aerosol distributions are not coincident with each other. The real CALIOP observations are very noisy because they are not yet averaged to either the CAD score resolution or the model resolution.

4 Evaluation tools

The importance of verification methods has been emphasized within the aerosol modeling community (cf. Benedetti et al., 2011). In this study, the data assimilation system was evaluated by the application of an object-based verification tool, the Method for Object-based Diagnostic Evaluation (MODE). We used aerosol optical thickness (AOT) as the analysis object of this MODE tool.

4.1 Traditional methods

Generally, model simulation (forecast) or data assimilation (analysis) results have been verified by the root-mean-squared error (RMSE), correlation scores, and skill scores, such as the probability of detection, false alarm ratio, and threat score. Indeed, the RMSE and correlation scores have performed very well when the verified quantity is continuous and does not exhibit sharp fluctuations. Consequently, numerical weather forecast models have been verified using the continuous fields as a proxy, such as temperature, pressure, and geopotential height. However, aerosol plumes are highly localized phenomena, are not continuous against the background field, and present extremely sharp fluctuations. The traditional verification methods, such as RMSE, correlation scores, and skill scores, are no use in aerosol forecast/analysis verification. As an example, Fig. 10 illustrates the difficulties associated with diagnosing analytical errors using traditional verification approaches. This figure shows various observation (O) and analysis (A) combinations, assuming that these crescent-shaped areas indicate homogeneous aerosol plumes, and the background concentrations are zero. The three combinations of Fig. 10a, b, and c yield the same RMSE and normal correlation. In contrast, the combination of Fig. 10d has the best RMSE performance. Unfortunately, traditional skill scores are unable to distinguish the performance differences in Fig. 10a, b and c. Subjectively, the combination in Fig. 10a appears to be a fairly good analysis that is merely offset somewhat to the right. In fact, for most of the aerosol researchers and product users, small location errors and small intensity errors are unimportant. Because aerosol distribution exhibits significant spatial variability, it is very difficult to simulate the structure and location of aerosol plumes. However, based on the comparison between an analysis grid and its counterpart observation grid, the traditional verification methods measure small errors at each grid point and penalize the performance of the analysis without diagnosing the small location or structure errors. A similar case can be observed in the verification of the precipitation forecast/analysis, in which rainfall is a local and episodic phenomenon similar to an aerosol outbreak.

Title Page

Abstract | Introduction

Conclusions | References

Tables | Figures

◄ | ►

◄ | ►

Back | Close

Full Screen / Esc

Printer-friendly Version

Interactive Discussion

To provide more diagnostic information about precipitation forecast performance and separate location errors from other errors, several approaches have been developed (e.g. Ebert and McBride, 2000; Casati et al., 2004; Davis et al., 2006a,b). The Method for Object-based Diagnostic Evaluation (MODE) is one of these approaches.

4.2 Method for object-based diagnostic evaluation

In a manner similar to the precipitation forecast verification, the aerosol analysis can be verified by object-based approaches, in which simulated and observed areas of aerosol plumes are represented and compared as objects through characterizations according to attributes such as location, size, and intensity. Of the object-based approaches, we utilized the MODE tool (Davis et al., 2006a,b), which was developed for the evaluation of precipitation forecasts from the Weather Research and Forecasting (WRF) model by the National Center for Atmospheric Research (NCAR). The MODE tool is included in the Model Evaluation Tools (MET) provided for the WRF community by NCAR (http://www.dtcenter.org/met/users/). This paper shows that MODE is applicable to evaluate the aerosol analyses obtained from model simulations and data assimilations.

MODE was developed to provide a tool with the ability to mimic a human eye's evaluation of model performance with the examination of graphical patterns. MODE includes the following multistep process to perceive two-dimensional graphical patterns:

Step (1) Identify objects,

Step (2) Measure the object attributes,

Step (3) Merge the objects in the same field,

Step (4) Match the objects from the analysis and observation fields,

Step (5) Compare the attributes of the analysis and the observation objects.

Full Screen / Esc

Printer-friendly Version

Interactive Discussion

The process that takes place between Steps 1 and 3 is illustrated with an example of precipitation distribution in Fig. 11. The first step is to convert the gridded values into simple objects using convolution (Fig. 11b) and a threshold mask (Fig. 11c). The convolution process smooths the raw data (from Fig. 11a to Fig. 11b) using a convolution filter; a threshold is then applied to generate the object borders (Fig. 11c). The original data values are restored to the object interiors (Fig. 11d). The outside of the objects is zeroed out. For this OSSE study, the convolution filter was a simple circular function with the averaging radius $R = 0.75$ model-grids, and the threshold was set to 0.2 aerosol optical thickness (AOT). The convolved field C_f is defined as

$$C_f(x,y) = \sum 1/\pi R^2 f_r(x - u, y - v), \text{if } x^2 + y^2 \leq R^2, \text{ and } C_f(x,y) = 0 \text{ otherwise,} \qquad (7)$$

where f_r is the raw data field, and the variables (x, y) and (u, v) are grid coordinates. When C_f is lower than the threshold, the grid is masked out.

The second step is to measure the object attributes defined by geometrical characteristics (such as the centroid location, size, axis angle, and aspect ratio) and other quantities (such as the 25th, 50th, 75th, and 90th percentile intensities) within each object. The third step is to merge the objects in the same field and match these objects between the observation field and the model field. While object merging is the process of associating objects in the same field to make a composite object, object matching is the process of associating objects in the observation field with objects in the model field. After this merging is complete, the attributes are recalculated (if desired) for the composite object in the same way before matching. In this step, the attributes include mutual quantities, such as centroid distance, object intersection, and union areas. The current version of MODE uses a fuzzy logic process – cf. the User's Guide of MET (NCAR DTC, 2012) – for both merging and matching objects. Once the object attributes are estimated, they are used as inputs in a fuzzy logic engine, in which interest maps I_i are defined for the individual attribute a_i with preconfigured parameters according to the a_i quantity, including distance, ratio, and intensity. The interest map ranges from zero (representing no interest) to one (highest interest). Additionally, confidence maps

OSSEs for satellite lidar observations

T. T. Sekiyama et al.

Full Screen / Esc

Printer-friendly Version

Interactive Discussion

S_i are defined for each attribute, reflecting how confident we are in the calculated value of an attribute. In MODE, all of the confidence maps except the map for the axis angle are constantly set to 1 (the axis angle confidence is a function of the aspect ratio). Next, we determine the weights w_i for each attribute to represent the relative impor-
5 tance of the attribute. In this OSSE study, centroid distance and boundary distance are weighted more heavily than other attributes because the locations of aerosol plumes that are close to each other should be the strongest indicator. Consequently, we calculate a single scalar number J integrating all the ingredients, as follows:

$$J = \sum w_i S_i(a_i) I_i(a_i) / \sum w_i S_i(a_i). \tag{8}$$

10 This judgment number J is then thresholded, and the pairs of objects with J values above the preconfigured threshold are merged (if they are in the same field, as shown in Fig. 11d) or matched (if they are in different fields). In the final step, we can compare the composite object attributes between the analysis and the observation: for example,
15 the distance between two object centroids; the ratio of the areas of two objects, defined as the lesser of the analysis area divided by the observation area or its reciprocal; and the ratio of the 75th percentile of intensity of the two objects, defined as the lesser of the analysis intensity divided by the observation intensity or its reciprocal. In short, the shorter the centroid distance, the better the experimental performance. The ratios
20 range from 1 (best) to 0 (worst). Additional details of MODE are described in NCAR DTC (2012) and by Davis et al. (2006a,b).

5 Results and discussion

The results of a standard test and various sensitivity tests are presented and discussed in this section. All the experiments were initiated at 00:00 UTC on 1 March 2007 and
25 terminated at 00:00 UTC on 1 June 2007. We validated the performance of these three-month experiments using MODE with sulfate and dust AOT distributions as the analysis objects.

5.1 Standard test

5.1.1 MODE scores

The standard-test experiment (Exp-Std) was conducted with 32 ensemble members, a 20 % covariance inflation, a 3000-km horizontal localization, 20 % observation errors,

5 a 2×10^{-5} m^{-1} data-screening threshold, the standard cloud-cover ratio, and one virtual satellite. The experimental result was validated against the Nature Run with respect to sulfate aerosol plumes and dust aerosol plumes. An example of the sulfate aerosol validation is presented in Fig. 12 with a validation of the free model run (FmR) without data assimilation. This comparison illustrates the superiority of the 4D-LETKF data

10 assimilation of satellite-borne lidar observations to the free-running simulation. In this example, the Exp-Std result (Fig. 12c) is in much closer agreement with the Nature Run (Fig. 12a) than the FmR result (Fig. 12b) to the human eye. However, the traditional scores exhibit nearly identical performances for both the FmR (RMSE = 0.33; normal correlation = 0.16) and the Exp-Std (RMSE = 0.34; normal correlation = 0.01). These

15 scores are summarized in Table 5. Although, in general, such a small correlation has no significance, the score of the Exp-Std is lower than that of the FmR. This is because the traditional verification methods only measure errors at each grid point and ignore the surrounding pattern. In contrast, the MODE scores indicate differences for the Exp-Std result and the FmR result, as shown in Fig. 12 and Table 5. The object centroid

20 distance of the Exp-Std result (1.51 grids) is less than half that of the FmR result (3.27 grids). One grid is approximately 280 km. The area ratio of the Exp-Std result is 0.70, while that of the FmR result is 0.41. Evidently, the MODE scores demonstrate the better performance of the Exp-Std, as measured by the human eye. The 75th-percentile intensity ratios of the Exp-Std (0.91) and the FmR (0.89) are nearly equivalent because

25 only part of the plumes (less than 25 % of the area) exhibits high AOT values among all the Nature Run, FmR, and Exp-Std results.

A similar result was obtained from the dust aerosol validation, as shown in Fig. 13 and Table 6. In this example, the Exp-Std result (Fig. 13c) demonstrates an evidently

closer agreement with the Nature Run (Fig. 13a) than the FmR result (Fig. 13b) to the human eye. The difference is, however, relatively small with the use of the traditional verification methods. While the normal correlation of the FmR result is negative (−0.41), that of the Exp-Std result is almost negligible (0.18). In contrast, the MODE

5   scores demonstrate the higher performance of the Exp-Std, as measured by the human eye. The object centroid distance of the Exp-Std result (0.86 grids) is 30 % smaller than that of the FmR result (1.22 grids). The area ratio is dramatically improved between the FmR result (0.44) and the Exp-Std result (0.76). On the other hand, the 75th-percentile intensity ratios are almost equivalent between the Exp-Std (0.89) and the FmR (0.86),

10 similar to the sulfate aerosol validation.

The time series of these MODE scores also demonstrate that the Nature Run is in closer agreement with the Exp-Std than the FmR result (Figs. 14 and 15). If two or more objects existed in a field in a day, these object attributes were averaged daily when plotting the time series. The field of analysis of sulfate aerosols was a region in East Asia

15 and the Northwest Pacific from 15° N to 52.5° N in latitude and from 90° E to 182.5° E in longitude, as shown in Fig. 12. This region frequently experiences extremely high sulfate concentrations. For the dust aerosols, the field of analysis was shifted to the Asian Dust region (from 20° N to 57.5° N in latitude and from 70° E to 162.5° E in longitude), primarily including China, Mongolia, Korea, and Japan, as shown in Fig. 13. First, the

20 three-month time series of sulfate aerosol validations are presented in Fig. 14a (centroid distance), Fig. 14b (area ratio), and Fig. 14c (75th-percentile intensity ratio). In the case of the centroid distance (Fig. 14a), although the difference between the FmR and the Exp-Std is negligible in March, the Exp-Std result exhibits a better performance in April and May. The three-monthly mean of the centroid distance is 2.15 grids for the

25 FmR and 1.45 grids for the Exp-Std. In the case of the area ratio (Fig. 14b), the Exp-Std result almost always exhibits a better performance during the three-month period. The three-monthly mean of the area ratio is 0.49 for the FmR and 0.76 for the Exp-Std. In the case of the 75th-percentile intensity ratio (Fig. 14c), the difference between the FmR and the Exp-Std is small, but the Exp-Std result almost always exhibits a better

performance during the three-month period. The three-monthly mean of the intensity ratio is 0.80 for the FmR and 0.85 for the Exp-Std. In summary, the MODE scores of the Exp-Std, i.e., the 4D-LETKF data assimilation results, are clearly superior to those of the FmR results.

Second, the three-month time series of dust aerosol validations are presented in Figs. 15a (centroid distance), 15b (area ratio), and 15c (75th-percentile intensity ratio). In the case of the centroid distance (Fig. 15a), the Exp-Std result exhibits a good performance in April and May. Unfortunately, MASINGAR tends to underestimate the dust outbreaks in March in Asian Dust source regions (Tanaka et al. 2011), so dust plumes are barely produced by either the Nature Run or the FmR. The three-monthly mean of the centroid distance is reduced from 2.59 grids of the FmR to 1.14 grids of the Exp-Std. For the area ratio (Fig. 15b), the Exp-Std result almost always exhibits its best performance in April and May. Particularly in May, the area ratio of the Exp-Std often presents values greater than 0.9, which means the area size is almost the same as in the Nature Run. The three-monthly mean of the area ratio is improved from 0.51 with the FmR to 0.72 with the Exp-Std. In the case of the 75th-percentile intensity ratio (Fig. 15c), the difference between the FmR and the Exp-Std is small, as seen in the sulfate aerosol validation, but the Exp-Std result almost always exhibits an equal or better performance during the three-month period. The three-monthly mean of the intensity ratio is 0.83 with the FmR, and 0.85 with the Exp-Std. In summary, these MODE scores indicate that the dust aerosol result of the Exp-Std, i.e., the 4D-LETKF data assimilation, is also superior to that of the FmR.

5.1.2 Flux verification

Flux estimation is one of the most important products of aerosol data assimilation, along with the plume distribution analysis described above. Therefore, we compared the surface dust emission flux of the Nature Run, the FmR result, and the Exp-Std results. As an example, Fig. 16 shows the surface dust emission accumulated during a dust event from 1 to 3 April 2007. In this plot, the dust weights of six size bins

from 0.200 µm to 3.17 µm in diameter were accumulated during the dust event period. Dust bins with a diameter of more than 3.17 µm were excluded because these large particles have an exponentially large mass ratio against smaller particles but a short lifetime in the model-grid scale. Unfortunately, the improvement caused by the data
5 assimilation is not clear in Fig. 16, and the Exp-Std result is slightly noisy. The Nature Run (Fig. 16a) and the FmR (Fig. 16b) have clearly different emission distributions in the arid regions along the border between China and Mongolia from the Gobi desert to the Taklamakan desert. A close inspection of these figures discloses that the data assimilation (Exp-Std: Fig. 16c) improves the overestimation in the Taklamakan desert
10 and the underestimation in the Gobi desert.

Although the horizontal pattern shows no clear advantage, the horizontal average is improved; i.e., the time series of the dust emission flux in the entire Asian Dust source region shows a large improvement. Figure 17a compares the Nature Run, the FmR, and the Exp-Std during the same period of Fig. 16, in which the dust emission is totaled
15 hourly in the rectangular region (35° N–50° N and 75° E–120° E) mainly covering China and Mongolia and including both the Gobi and Taklamakan deserts. The dust weights of six size bins from 0.200 µm to 3.17 µm in diameter were also accumulated here. In Fig. 17a, the overestimation on 2 April is dramatically improved by the data assimilation that day. In this case, the Exp-Std data assimilation was able to perfectly adjust the total
20 amount of dust emission, but it did not properly allocate it to each grid point. In contrast, the extreme underestimation of the afternoon of 31 March was not improved at all.

Another example of the time series of dust emission flux totals from the Asian Dust source region is presented in Fig. 18a. This is the case in late May 2007, which corresponded to a severe dust storm in the real world. The region and the accumulated dust
25 size are the same as in the case depicted in Fig. 17a. In this period, large dust outbreaks occurred seven times. Among them, the third (26 May) and seventh (30 May) outbreaks were almost perfectly adjusted. The first (24 May), second (25 May), and fifth (28 May) outbreaks were not improved at all. The sixth (29 May) outbreak was improved but not enough. The fourth (27 May) outbreak was deteriorated; however, the

FmR originally provides a good agreement with the Nature Run. It is notable that dust emission estimation is more difficult than plume location estimation because emission estimation is impossible if the emitted dust plume is not observed in the downwind direction within 24 h. In contrast, there are multiple chances for plume location estimation to detect the plume for more than 24 h.

Consequently, we examined another test experiment (Exp-4sat) with four satellites emulating CALIPSO. The Exp-4sat had the same experiment settings as the Exp-Std, with the exception of the number of satellites. In Exp-4sat, each satellite circled the Earth along the CALIPSO orbit track, $\pi/2$-phase-shifting away from both the preceding and following satellites so that the observational cover area was nearly quadrupled. The results of the Exp-4sat is presented in Figs. 17b and 18b. Among the seven dust outbreaks depicted in Fig. 18, the first (24 May), fourth (27 May), and sixth (29 May) outbreaks were remarkably improved by the Exp-4sat (Fig. 18b) in comparison with the Exp-Std (Fig. 18a). Furthermore, the second (25 May) and fifth (28 May) outbreaks were also improved by the Exp-4sat although not perfect. In contrast, the extreme underestimation of the afternoon of 31 March in Fig. 17b was not improved by the Exp-4sat. In this case, it is difficult for the multiplicative dust emission factor α_{ij} in Eq. (2) to correct the dust emission intensity because the first-guess intensity in the data assimilation process (the same as the FmR result) is almost zero. In our multiplicative scheme, a zero emission cannot be perturbed and modified. In addition, the dust emission factor α_{ij} is constant for one analysis cycle of 24 h from 00:00 UTC to 24:00 UTC. If the first guess (FmR) overestimates in the morning and underestimates in the afternoon, similar to the event on 31 March in Fig. 17, it is impossible to adjust the factor correctly for both. The MODE scores of the Exp-4sat are presented in Tables 7 (sulfate aerosol) and 8 (dust aerosol). Although the dust emission estimation was improved by the increase in the number of satellites, the dust plume analysis was not improved or was deteriorated. This is probably due to the strongly constrained meteorological field and the consequent limitation of the freedom to control the aerosol variables.

Full Screen / Esc

Printer-friendly Version

Interactive Discussion

5.2 Sensitivity tests

To validate the robustness of the 4D-LETKF data assimilation system and determine the most suitable experimental settings for this system, sensitivity-test experiments were conducted with the conditions shown in Table 4. Their results are listed in Tables 7 and 8 with the results of the FmR and the Exp-Std. These results are presented as a three-monthly mean of each MODE score derived from the sulfate or dust AOT distribution.

5.2.1 Ensemble size test

We have tested different values of the ensemble size. Although the standard size was 32 members, the sensitivity-test experiments were performed with 128 members (Exp-Ens128), 64 members (Exp-Ens64), 16 members (Exp-Ens32), or 8 members (Exp-Ens8). For the sulfate aerosol, as shown in Table 7, the ensemble-size experiments did not differ much in comparison with the Exp-Std, with the exception of the centroid distance of Exp-ens8, which was slightly worse than the others. For dust aerosol, as shown in Table 8, the best performance was demonstrated by the Exp-Std with 32 members; the second was demonstrated by the Exp-Ens64; and the worst was produced by the Exp-Ens8. The Exp-Ens128 did not exhibit the best performance. It was found that the use of a too-small ensemble size, such as 8 members, deteriorates the confidence of the data assimilation in spite of the fact the ensemble size does not influence the performance of data assimilation much. This is probably because this data assimilation is constrained by the meteorological field nudged into the reanalysis, so the degree of freedom to control aerosol variables is limited in the data assimilation.

5.2.2 Covariance inflation and localization scale test

We have tested different values of the covariance inflation factor and the localization scale. First, while the standard inflation was 20 %, the inflation-sensitivity-test

experiments were performed using 5 % (Exp-Inf05), 10 % (Exp-Inf10), and 40 % (Exp-Inf40) inflation. For sulfate aerosol, the results of these sensitivity experiments did not display a clear difference in comparison with that of the Exp-Std, as shown in Table 7. In contrast, for dust aerosol, the best performance was exhibited by the Exp-Std when the centroid distance was used as a measure or by the Exp-Inf40 when the area ratio was used as a measure, as shown in Table 8. The worst performance was exhibited by the Exp-Inf05. The use of small covariance inflation factors tended to deteriorate the confidence of the data assimilation. However, inflation factors of more than 40 % caused divergences in the data assimilation (not shown in the tables). Second, the sensitivity-test experiment of the localization scale was conducted at 1000 km (Exp-Lcl1000), while the standard localization scale was 3000 km. For sulfate aerosol, the results of the Exp-Lcl1000 were almost equal to or slightly worse than that of the Exp-Std, as shown in Table 7. In contrast, for dust aerosol, the shorter localization scale (1000 km) evidently worsened the data assimilation performance in comparison with the standard localization scale (3000 km), as shown in Table 8. This is probably because a localization scale of 1000 km is large enough to optimize aerosol plume distribution, but it is too short to conversely optimize the aerosol flux intensity. In this study, sulfur sources are not controlled by the data assimilation, but dust sources are controlled in this manner. Dust aerosol distributions depend strongly on the dust emission flux.

5.2.3 Observation error test

We also tested different values of the observation errors. While the standard observation error was 20 % with a minimum of $1 \times 10^{-4}\,\mathrm{sr}^{-1}\,\mathrm{km}^{-1}$, the sensitivity-test experiments were performed with 40 % error and a minimum of $2 \times 10^{-4}\,\mathrm{sr}^{-1}\,\mathrm{km}^{-1}$ (Exp-2err) and 100 % with a minimum of $5 \times 10^{-4}\,\mathrm{sr}^{-1}\,\mathrm{km}^{-1}$ (Exp-5err). For sulfate aerosol, the results of these sensitivity experiments exhibited few differences from those of the Exp-Std, as shown in Table 7. For dust aerosol, however, while the result of the Exp-2err was almost equal to or slightly better than that of the Exp-Std, the result of the Exp-5err was

worse than that of the Exp-Std, as shown in Table 8. For the real CALIPSO/CALIOP, a 20 % observation error is assumed (Winker et al., 2007), but the error is not statistically significant because the observations of the aerosol remote sensing instruments exhibit a large discrepancy with one another (e.g. Chapter 2 of IPCC, 2007; Schuster et al., 2012). Thus, a 40 % observation error appears to be within the expectable range, and it is, therefore, favorable that the 4D-LETKF data assimilation system with CALIPSO/CALIOP observations works very well with a 40 % observation error. On the other hand, it is determined that this system does not work with a too-large observation error, such as 100 %.

5.2.4 Data density test

We also tested different conditions of fractional cloudiness and the data-screening threshold. These two conditions influence the observational data density. First, the cloudiness-sensitivity-test experiments were performed using a perfectly clear sky (Exp-Sky), a more cloudy sky (0.1 × clear sky probability; Exp-Cld01), and a much more cloudy sky (0.05 × clear sky probability; Exp-Cld005). In comparison with the Exp-Std, the Exp-Sky has approximately double the amount of data; the Exp-Cld01 has approximately 1/6 the amount of data; and Exp-Cld005 has approximately 1/12 the amount of data. For sulfate aerosol, the results of these sensitivity experiments exhibited few differences from those of the Exp-Std, as shown in Table 7. In contrast, the dust aerosol results exhibited the following features, as shown in Table 8: the Exp-Sky performance was slightly superior to the Exp-Std performance; the Exp-Cld01 performance was almost equal to the Exp-Std performance; and the Exp-Cld005 performance was slightly inferior to the Exp-Std performance. This means that the 4D-LETKF data assimilation system is very robust even when there is a smaller amount of observation data. However, it is notable that this sensitivity test scheme is multiplicative for the amount of clouds; thus, the clear skies are always clear, even in the Exp-Cld01 or Exp-Cld005. Second, the sensitivity-test experiment of the data-screening threshold was conducted with a threshold of $1 \times 10^{-4}\,\mathrm{m}^{-1}$ (Exp-Hth) that was five times higher than the standard

Full Screen / Esc

Printer-friendly Version

Interactive Discussion

threshold ($2 \times 10^{-5}\,\mathrm{m}^{-1}$). In comparison with the Exp-Std, the Exp-Hth had approximately 1/8 the amount of data. For sulfate aerosol, the result of the Exp-Hth was almost equal to that of the Exp-Std, as shown in Table 7. In contrast, for dust aerosol, the higher threshold greatly diminished the data assimilation performance in comparison with the standard threshold, as shown in Table 8. This Exp-Hth result for dust aerosol had the worst centroid distance among the sensitivity-test experiments. This result implies that aerosol discrimination before the data assimilation process has a large impact on the data assimilation performance. Quality matters more than quantity. The data amount of the Exp-Hth (1/6) is larger than that of the Exp-Cld01 (1/8), but the performance of the Exp-Cld01 is better than that of the Exp-Hth.

6 Conclusions

An ensemble-based data assimilation approach has been investigated with simulated satellite-borne lidar aerosol observations using the OSSE technique. In the OSSEs, CALIPSO/CALIOP aerosol observations were simulated, accounting for cloudiness. An object-based verification tool called MODE was used to evaluate the data assimilation results, concentrating on East Asia. Consequently, it was found that the 4D-LETKF aerosol data assimilation system (Sekiyama et al., 2010, 2011b) had the ability to produce a better analysis of sulfate and dust aerosols than a free-running simulation model. The three-monthly mean centroid distance (from the "truth") of aerosol plumes was improved from 2.15 grids ($\approx 600\,\mathrm{km}$) to 1.45 grids ($\approx 400\,\mathrm{km}$) for sulfate aerosols and from 2.59 grids ($\approx 750\,\mathrm{km}$) to 1.14 grids ($\approx 330\,\mathrm{km}$) for dust aerosols. The three-monthly mean area ratio (to the "truth") of aerosol plumes was improved from 0.49 to 0.76 for sulfate aerosols and from 0.51 to 0.72 for dust aerosols. The satellite-borne lidar data assimilation successfully improved both the aerosol analysis and the dust emission estimation in the OSSEs.

This OSSE study is the first in which satellite-borne lidar Level 1B data were emulated and assimilated successfully. This result clearly indicated that it is possible to

assimilate attenuated backscattering coefficients and depolarization ratios using a non-linear observation operator; i.e., the retrieval process was unnecessary to obtain the extinction coefficients. In addition, this successful result indicated great possibilities for the beneficial use of horizontally sparse but vertically/temporally dense information, such as lidar observations, when coupled with a four-dimensional data assimilation system. It has been difficult for the human eye to address horizontally sparse observations without data assimilation. Although some technical difficulties and limitations of OSSEs were revealed, we demonstrated that the OSSEs could play an important role in the assessment of a novel data assimilation system and a new observing system, even at the planning stage. The same data assimilation system and verification approach can probably be applied to regions other than East Asia and to species other than sulfate and dust aerosols. For example, we intend to validate the analysis of Saharan dust aerosol in the near future.

We explored the optimal parameter settings of inflation and localization for the LETKF algorithm and assessed the robustness of this data assimilation system against a decrease in ensemble members and the number of observations using sensitivity tests. Consequently, we found better experimental settings of the 4D-LETKF data assimilation system . Meanwhile, we did not observe the expected large differences between the results of these sensitivity tests. This is probably because this data assimilation is constrained by the meteorological field nudged to the reanalysis, so the degree of the freedom to control the aerosol variables is limited in the data assimilation. In the sensitivity tests, the dust analyses were more sensitive to several experimental condition settings (i.e., observation error, localization scale, and data density) than were the sulfate analyses. This is probably because the dust aerosol distribution is strongly influenced by both the meteorological circumstances and the accuracy of the dust emission estimation controlled by the data assimilation. Therefore, if a setting in the sensitivity-test experiments deteriorates the dust analyses, the setting is probably an obstructive factor in the inverse estimation of dust emission flux. While the dust emission estimation was improved by an increase in the number of satellites from one CALIPSO

(Exp-Std) to four CALIPSOs (Exp-4sat), the dust plume analysis of the Exp-4sat did not exhibit a great difference; in fact, it was slightly worse than that of the Exp-Std. This is also probably due to the strongly constrained meteorological field and the limitation of the freedom to control the aerosol variables. Further improvements are expected to
5 emerge from the simultaneous assimilation of aerosol observations with meteorological observations, as suggested by Kang et al. (2011) for CO_2 data assimilation using OSSEs.

This study has demonstrated the beneficial results of data assimilation, but it should be noted that these experiments used the OSSEs in which everything was ideally sim-
10 ulated. However, the 4D-LETKF data assimilation system worked successfully under experimental conditions that were configured more strictly than the real observational conditions, including cloudiness and observation errors. In spite of the many controversies regarding OSSEs, this study demonstrates that carefully constructed OSSEs are able to provide useful information for the verification of a data assimilation system
15 and observing systems. The results presented in this paper strongly suggest that the 4D-LETKF data assimilation system of the real CALIPSO data have a beneficial impact on the development of dust and sulfate aerosol analyses. Furthermore, the use of the OSSE technique demonstrated here will allow us to perform a prior assessment of the next-generation lidar satellite EarthCARE, which will be launched in 2015 by the
20 European Space Agency (ESA) and the Japan Aerospace eXploration Agency (JAXA).

OSSEs for satellite lidar observations

T. T. Sekiyama et al.

References

Andersson, E. and Masutani, M.: Collaboration on observing system simulation experiments (Joint OSSE), ECMWF Newslett., 123, 14–16, 2010.

Atlas, R.: Atmospheric observations and experiments to assess their usefulness in data assimilation, J. Meteor. Soc. Japan, 75, 111–130, 1997.

Benedetti, A., Morcrette, J.-J., Boucher, O., Dethof, A., Engelen, R., Fisher, M., Flentje, H., Huneeus, N., Jones, L., Kaiser, J., Kinne, S., Mangold, A., Razinger, M., Simmons, A., and Suttie, M.: Aerosol analysis and forecast in the European Centre for Medium-Range Weather Forecasts Integrated Forecast System: 2. data assimilation, J. Geophys. Res., 114, D13205, doi:10.1029/2008JD011115, 2009.

Benedetti, A., Reid, J. S., and Colarco, P. R.: International cooperative for aerosol prediction workshop on aerosol forecast verification, Bull. Am. Meteorol. Soc., 92, ES48–ES53, 2011.

Bishop, C. H., Etherton, B. J., and Majumdar, S. J.: Adaptive sampling with the ensemble transform Kalman filter. Part I: Theoretical aspects, Mon. Weather Rev., 129, 420–436, 2001.

Bouttier, F. and Courtier, P.: Data Assimilation Concepts and Methods, Meteorological Training Course Lecture Series, ECMWF, Reading, UK, 75 pp., 1999.

Casati, B., Ross, G., and Stephenson, D. B.: A new intensity-scale approach for the verification of spatial precipitation forecasts, Meteorol. Appl., 11, 141–154, 2004.

Chin, M., Ginoux, P., Kinne, S., Torres, O., Holben, B. N., Duncan, B. N., Martin, R. V., Logan, J. A., Higurashi, A., and Nakajima, T.: Tropospheric aerosol optical thickness from the GOCART model and comparisons with satellite and sun photometer measurements, J. Atmos. Sci., 59, 461–483, 2002.

Collins, W., Rasch, P., Eaton, B., Khattatov, B., and Lamarque, J. F.: Simulating aerosols using a chemical transport model with assimilation of satellite aerosol retrievals: methodology for INDOEX, J. Geophys. Res., 106, 7313–7336, 2001.

Davis, C., Brown, B., and Bullock, R.: Object-based verification of precipitation forecasts. Part I: Methodology and application to mesoscale rain areas, Mon. Weather Rev., 134, 1772–1784, 2006a.

Davis, C., Brown, B., and Bullock, R.: Object-based verification of precipitation forecasts. Part II: Application to convective rain systems, Mon. Weather Rev., 134, 1785–1795, 2006b.

Ebert, E. E. and McBride, J. L.: Verification of precipitation in weather systems: determination of systematic errors, J. Hydrology, 239, 179–202, 2000.

OSSEs for satellite lidar observations

T. T. Sekiyama et al.

Evensen, G.: Sequential data assimilation with a nonlinear quasigeostrophic model using Monte Carlo methods to forecast error statistics, J. Geophys. Res., 99, 10143–10162, 1994.

Generoso, S., Breon, F., Chevallier, F., Balkanski, Y., Schulz, M., and Bey, I.: Assimilation of POLDER aerosol optical thickness into the LMDz-INCA model: implications for the artic aerosol burden, J. Geophys. Res., 112, D02311, doi:10.1029/2005JD006954, 2007.

Greeley, R. and Iversen, J. D.: Wind as a geological process, No. 4 in: Cambridge Planetary Science Series, Cambridge University Press, New York, USA, 348 pp., 1985.

Hunt, B. R., Kalnay, E., Kostelich, E. J., Ott, E., Patil, D. J., Sauer, T., Szunyogh, I., Yorke, J. A., and Zimin, A. V.: Four-dimensional ensemble Kalman filtering, Tellus A, 56, 273–277, 2004.

Hunt, B. R., Kostelich, E. J., and Szunyogh, I.: Efficient data assimilation for spatiotemporal chaos: a local ensemble transform Kalman filter, Physica D, 230, 112–126, 2007.

Intergovernmental Panel on Climate Change (IPCC): Changes in Atmospheric Constituents and in Radiative Forcing, in: Climate Change 2007: The Physical Science Basis. Contribution of Working Group I to the Fourth Assessment Report of the Intergovernmental Panel on Climate Change, edited by: Solomon, S., et al., Cambridge University Press, Cambridge, UK and New York, NY, USA, 996 pp., 2007.

Kalman, R. E.: A new approach to linear filtering and prediction problems, J. Basic Eng., 82, 35–45, 1960.

Kalnay, E.: Ensemble Kalman filter: current status and potential, in: Data Assimilation: Making Sense of Observations, edited by: Lahoz, W., et al., Springer, Heidelberg, Germany, 69–92, 2010.

Kalnay, E., Li, H. Miyoshi, T., YANG, S. C., and Ballabrera-Poy, J.: 4D-Var or ensemble Kalman filter?, Tellus A, 59, 758–773, 2007.

Kang, J. S., Kalnay, E., Liu, J., Fung, I., Miyoshi, T., and Ide, K.: "Variable localization" in an ensemble Kalman filter: application to the carbon cycle data assimilation, J. Geophys. Res., 116, D09110, doi:10.1029/2010JD014673, 2011.

Lahoz, W., Khattatov, B., and Menard, R.: Data Assimilation Making Sense of Observations, Springer, Berlin, Germany, 718 pp., 2010.

Lewis, J. M., Lakshmivarahan, S., and Dhall, S. K.: Dynamic Data Assimilation: A Least Squares Approach, Cambridge University Press, Cambridge, UK and New York, NY, USA, 654 pp., 2006.

Lin, C., Wang, Z., and Zhu, J.: An Ensemble Kalman Filter for severe dust storm data assimilation over China, Atmos. Chem. Phys., 8, 2975–2983, doi:10.5194/acp-8-2975-2008, 2008a.

OSSEs for satellite lidar observations

T. T. Sekiyama et al.

|◄ | ►|

◄ | ►

Back | Close

Full Screen / Esc

Printer-friendly Version

Interactive Discussion

Discussion Paper | Discussion Paper | Discussion Paper | Discussion Paper | Discussion Paper

Lin, C., Zhu, J., and Wang, Z.: Model bias correction for dust storm forecast using ensemble Kalman filter, J. Geophys. Res., 113, D14306, doi:10.1029/2007JD009498, 2008b.

Liu, Z., Vaughan, M. A., Winker, D. M., Hostetler, C. A., Poole, L. R., Hlavka, D., Hart, W., and McGill, M.: Use of probability distribution functions for discriminating between cloud and aerosol in lidar backscatter data, J. Geophys. Res., 109, D15202, doi:10.1029/2004JD004732, 2004.

Liu, J., and Kalnay, E.: Simple Doppler wind lidar adaptive observation experiments with 3D-Var and an ensemble Kalman filter in a global primitive equations model, Geophys. Res. Lett., 34, L19808, doi:10.1029/2007GL030707, 2007.

Lorenc, A. C.: A global three-dimensional multivariate statistical interpolation scheme, Mon. Weather Rev., 109, 701–721, 1981.

Masutani, M., Schlatter, T. W., Errico, R. M., Stoffelen, A., Andersson, E., Lahoz, W., Woolen, J. S., Emmitt, G. D., Riishojgaard, L.-P., and Lord, S. J.: Observing System Simulation Experiments, Data Assimilation: Making Sense of Observations, edited by: Lahoz, W., et al., Springer, Heidelberg, Germany, 647–679, 2010a.

Masutani, M., Woolen, J. S., Lord, S. J., Emmitt, G. D., Kleespies, T. J., Wood, S. A., Greco, S., Sun, H, Terry, J., Kapoor, V., Treadon, R., and Campana, K. A.: Observing system simulation experiments at the National Centers for Environmental Prediction, J. Geophys. Res., 115, D07101, doi:10.1029/2009JD012528, 2010b.

Miyazaki, K., Maki, T., Patra, P., and Nakazawa, T.: Assessing the impact of satellite, aircraft, and surface observations on CO_2 flux estimation using an ensemble-based 4-D data assimilation system, J. Geophys. Res., 116, D16306, doi:10.1029/2010JD015366, 2011.

Miyoshi, T. and Aranami, K.: Applying a four-dimensional local ensemble transform Kalman filter (4D-LETKF) to the JMA nonhydrostatic model (NHM), SOLA, 2, 128–131, doi:10.2151/sola.2006-033, 2006.

Miyoshi, T. and Yamane, S.: Local ensemble transform Kalman filtering with an AGCM at a T159/L48 resolution, Mon. Weather Rev., 135, 3841–3861, 2007.

Miyoshi, T., Yamane, S., and Enomoto, T.: Localization the error covariance by physical distances within a Local Ensemble Transform Kalman Filter (LETKF), SOLA, 3, 089–092, doi:10.2151/sola.2007-023, 2007.

Nakicenovic, N. and Swart, R. (Eds.): Special Report on Emissions Scenarios, Cambridge University Press, Cambridge, UK, 612 pp., 2000.

OSSEs for satellite lidar observations

T. T. Sekiyama et al.

Title Page

Abstract	Introduction
Conclusions	References
Tables	Figures

◄◄ ►►

◄ ►

Back Close

Full Screen / Esc

Printer-friendly Version

Interactive Discussion

NCAR Developmental Testbed Center (DTC): Model Evaluation Tools Version 3.1 (METv3.1) User's Guide 3.1, available at: http://www.dtcenter.org/met/users/docs/users_guide/MET_Users_Guide_v3.1.pdf (last access: 20 July 2012), 2012.

Niu, T., Gong, S. L., Zhu, G. F., Liu, H. L., Hu, X. Q., Zhou, C. H., and Wang, Y. Q.: Data assimilation of dust aerosol observations for the CUACE/dust forecasting system, Atmos. Chem. Phys., 8, 3473–3482, doi:10.5194/acp-8-3473-2008, 2008.

Owen, P. R.: Saltation of uniform grains in air, J. Fluid Mech., 20, 225–242, 1964.

PPark, S. K. and Xu, L.: Data Assimilation for Atmospheric, Oceanic and Hydrologic Applications, Springer, Berlin, Germany, 475 pp., 2009.

Raisanen, P.: Effective longwave cloud fraction and maximum-random overlap of clouds: a problem and a solution, Mon. Weather Rev., 126, 3336–3340, 1998.

Schuster, G. L., Vaughan, M., MacDonnell, D., Su, W., Winker, D., Dubovik, O., Lapyonok, T., and Trepte, C.: Comparison of CALIPSO aerosol optical depth retrievals to AERONET measurements, and a climatology for the lidar ratio of dust, Atmos. Chem. Phys. Discuss., 12, 11641–11697, doi:10.5194/acpd-12-11641-2012, 2012.

Schutgens, N. A. J., Miyoshi, T., Takemura, T., and Nakajima, T.: Applying an ensemble Kalman filter to the assimilation of AERONET observations in a global aerosol transport model, Atmos. Chem. Phys., 10, 2561–2576, doi:10.5194/acp-10-2561-2010, 2010.

Sekiyama, T. T., Tanaka, T. Y., Shimizu, A., and Miyoshi, T.: Data assimilation of CALIPSO aerosol observations, Atmos. Chem. Phys., 10, 39–49, doi:10.5194/acp-10-39-2010, 2010.

Sekiyama, T. T., Deushi, M., and Miyoshi, T.: Operation-oriented ensemble data assimilation of total column ozone, SOLA, 7, 41–44, 2011a.

Sekiyama, T. T., Tanaka, T. Y., Maki, T., and Mikami, M.: The effects of snow cover and soil moisture on Asian dust: II. Emission estimation by Lidar data assimilation, SOLA, 7A, 40–43, doi:10.2151/sola.7A-011, 2011b.

Shao, Y. and Lu, H.: A simple expression for wind erosion threshold friction velocity, J. Geophys. Res., 105, 22437–22443, 2000.

Shibata, K., Yoshimura H., Ohizumi, M., Hosaka, M. and Sugi, M.: A simulation of troposphere, stratosphere and mesosphere with an MRI/JMA98GCM, Pap. Meteor. Geophys., 50, 15–53, 1999.

Shimizu, A., Sugimoto, N., Matsui, I., Arao, K., Uno, I., Murayama, T., Kagawa, N., Aoki, K., Uchiyama, A., and Yamazaki, A.: Continuous observations of Asian dust and other aerosols

OSSEs for satellite lidar observations

T. T. Sekiyama et al.

Title Page

Abstract | Introduction

Conclusions | References

Tables | Figures

Back | Close

Full Screen / Esc

Printer-friendly Version

Interactive Discussion

Discussion Paper | Discussion Paper | Discussion Paper | Discussion Paper

by polarization lidars in China and Japan during ACE-Asia, J. Geophys. Res., 109, D19S17, doi:10.1029/2002JD003253, 2004.

Tanaka, T. Y. and Chiba, M.: Global simulation of dust aerosol with a chemical transport model, MASINGAR, J. Meteorol. Soc. Jpn., 83A, 255–278, 2005.

Tanaka, T. Y. and Chiba, M.: A numerical study of the contributions of dust source regions to the global dust budget, Global Planet. Change, 52, 88–104, doi:10.1016/j.gloplacha.2006.02.002, 2006.

Tanaka, T. Y., Orito, K., Sekiyama, T. T., Shibata, K., Chiba, M., and Tanaka, H.: MASINGAR, a global tropospheric aerosol chemical transport model coupled with MRI/JMA98 GCM, Pap. Met. Geophys., 53, 119–138, 2003.

Tanaka, T. Y., Kurosaki, Y., Chiba, M., Matsumura, T., Nagai, T., Yamazaki, A., Uchiyama, A., Tsunematsu, N., and Kai, K.: Trans-continental dust transport from North Africa and the Middle East to East Asia, Atmos. Environ., 39, 3901–3909, 2005.

Tanaka, T. Y., Aoki, T., Takahashi, H., Shibata, K., Uchiyama, A., and Mikami, M.: Study of the sensitivity of optical properties of mineral dust to the direct aerosol radiative perturbation using a global aerosol transport model, SOLA, 3, 33–36, doi:10.2151/sola.2007-009, 2007.

Tanaka, T. Y., Sekiyama, T. T., Maki, T., and Mikami, M.: The effects of snow cover and soil moisture on Asian dust: I. a numerical sensitivity study, SOLA, 7A, 036–039, doi:10.2151/sola.7A-010, 2011.

Tombette, M., Mallet, V., and Sportisse, B.: PM_{10} data assimilation over Europe with the optimal interpolation method, Atmos. Chem. Phys., 9, 57–70, doi:10.5194/acp-9-57-2009, 2009.

United Nations Environment Programme (UNEP): Atmospheric Brown Clouds Regional Assessment Report with Focus on Asia, UNEP, Nairobi, Kenya, 354 pp., 2008.

Uno, I., Wang, Z., Chiba, M., Chun, Y. S., Gong, S. L., Hara, Y., Jung, E., Lee, S. S., Liu, M., Mikami, M., Music, S., Nickovic, S., Satake, S., Shao, Y., Song, Z., Sugimoto, N., Tanaka, T., and Westphal, D. L.: Dust model intercomparison (DMIP) study over Asia: overview, J. Geophys. Res., 111, D12213, doi:10.1029/2005JD006575, 2006.

White, B. R.: Soil transport by winds on Mars, J. Geophys. Res., 84, 4643–4651, 1979.

Winker, D. M., Hunt, H. H., and McGill, M. J.: Initial performance assessment of CALIOP, Geophys. Res. Lett., 34, L19803, doi:10.1029/2007GL030135, 2007.

World Health Organization (WHO) Regional Office for Europe: Air Quality Guidelines Global Update 2005: Particulate matter, ozone, nitrogen dioxide and sulfur dioxide, WHO Regional Office for Europe, Copenhagen, Denmark, 2006.

OSSEs for satellite lidar observations

T. T. Sekiyama et al.

Yang, S., Kalnay, E., and Hunt, B.: Handling nonlinearity in an Ensemble Kalman Filter: experiments with the three-variable Lorenz model, Mon. Weather Rev., online first, doi:10.1175/MWR-D-11-00313.1, 2012.

Yu, H., Dickinson, R., Chin, M., Kaufman, Y., Holben, B., Geogdzhayev, I., and Mishchenko, M.: Annual cycle of global distributions of aerosol optical depth from integration of MODIS retrievals and GOCART model simulations, J. Geophys. Res., 108, 4128, doi:10.1029/2002JD002717, 2003.

Yumimoto, K., Uno, I., Sugimoto, N., Shimizu, A., Liu, Z., and Winker, D. M.: Adjoint inversion modeling of Asian dust emission using lidar observations, Atmos. Chem. Phys., 8, 2869–2884, doi:10.5194/acp-8-2869-2008, 2008.

Zhang, J., Reid, J. S., Westphal, D. L., Baker, N. L., and Hyer, E. J.: A system for operational aerosol optical depth data assimilation over global oceans, J. Geophys. Res., 113, D10208, doi:10.1029/2007JD009065, 2008.

OSSEs for satellite lidar observations

T. T. Sekiyama et al.

Table 1. Properties of aerosol particles in MASINGAR. Volume mean diameters (Dv) are shown for each size bin of dust aerosol.

Type	Size bin	Density (g cm^{-3})	Diameter (µm)	Dv (µm)
Dust	1	2.50	0.200–0.317	0.271
	2	2.50	0.317–0.502	0.430
	3	2.50	0.502–0.796	0.681
	4	2.50	0.796–1.26	1.08
	5	2.50	1.26–2.00	1.71
	6	2.65	2.00–3.17	2.71
	7	2.65	3.17–5.02	4.30
	8	2.65	5.02–7.96	6.81
	9	2.65	7.96–12.6	10.8
	10	2.65	12.6–20.0	17.1
Sulfate		1.77	0.30	
Organic carbon		1.50	0.36	
Black carbon		1.25	0.36	
Sea-salt	1–10	2.25	0.200–20.0	0.271–17.1

Full Screen / Esc

Printer-friendly Version

Interactive Discussion

Table 2. Complex index of refraction of each aerosol species at 532 nm and 1064 nm.

| | Complex index of refraction | | | |
| | $\lambda = 532\,nm$ | | $\lambda = 1064\,nm$ | |
Type	Real part	Imaginary part	Real part	Imaginary part
Dust	1.67	8.1×10^{-3}	1.63	1.9×10^{-6}
Sulfate	1.43	1.0×10^{-8}	1.42	1.5×10^{-6}
Organic carbon	1.53	5.0×10^{-3}	1.53	5.0×10^{-3}
Black carbon	1.75	0.45	1.75	0.44
Sea-salt	1.50	1.0×10^{-8}	1.47	2.0×10^{-4}

OSSEs for satellite lidar observations

T. T. Sekiyama et al.

Table 3. Hygroscopic growth factors as a function of relative humidity (Chin et al., 2002).

RH (%)	0	50	70	80	90	95	99
Sulfate	1.0	1.4	1.5	1.6	1.8	1.9	2.2
Organic carbon	1.0	1.2	1.4	1.5	1.6	1.8	2.2
Black carbon	1.0	1.0	1.0	1.2	1.4	1.5	1.9
Sea-salt	1.0	1.6	1.8	2.0	2.4	2.9	4.8

Table 4. Experimental conditions of the standard and sensitivity tests.

Experiment	Condition
Exp-Std	Standard test (ensemble size = 32, covariance inflation = 20 %, horizontal localization = 3000 km, observation error = 20 %)
Exp-Ens128	Ensemble size = 128 members
Exp-Ens64	Ensemble size = 64 members
Exp-Ens16	Ensemble size = 16 members
Exp-Ens8	Ensemble size = 8 members
Exp-Inf05	Covariance inflation = 5 %
Exp-Inf10	Covariance inflation = 10 %
Exp-Inf40	Covariance inflation = 40 %
Exp-Lcl1000	Horizontal localization = 1000 km
Exp-2err	Two-fold observation error (40 %)
Exp-5err	Five-fold observation error (100 %)
Exp-Sky	Perfectly clear sky ($\approx$ double data amount)
Exp-Cld01	Cloudy: 0.1-fold clear sky probability ($\approx$ 1/6 data amount)
Exp-Cld005	Cloudy: 0.05-fold clear sky probability ($\approx$ 1/12 data amount)
Exp-Hth	Higher noise threshold ($\approx$ 1/8 data amount)
Exp-4sat	4 satellites used

Table 5. Traditional and object-based verification scores of sulfate aerosol shown in Fig. 12.

	Scores	Sulfate aerosol on May 11	
		Free model run	Data assimilation
Traditional	RMSE (0 is best; ∞ is worst)	**0.33**[*]	0.34
	Correlation (1 is best; 0 is worst)	**0.16**[*]	0.01
Object-based (MODE)	Centroid distance (0 is best; ∞ is worst)	3.27	**1.51**[*]
	Area Ratio (1 is best; 0 is worst)	0.41	**0.70**[*]
	75th Intensity Ratio (1 is best; 0 is worst)	0.89	**0.91**[*]

[*] Bold values indicate better scores between the free model run and the data assimilation.

Table 6. Traditional and object-based verification scores of the dust aerosol shown in Fig. 13.

	Scores	Dust aerosol on May 16	
		Free model run	Data assimilation
Traditional	RMSE (0 is best; ∞ is worst)	**0.31**[1]	0.16
	Correlation (1 is best; 0 is worst)[2]	−0.41	0.18
Object-based (MODE)	Centroid distance (0 is best; ∞ is worst)	1.22	**0.86**[1]
	Area ratio (1 is best; 0 is worst)	0.44	**0.76**[1]
	75th intensity ratio (1 is best; 0 is worst)	0.86	**0.89**[1]

[1] Bold values indicate better scores between the free model run and the data assimilation.
[2] A controversy might exist over which is the worst correlation, 0 or −1.

Table 7. Performance of the sulfate aerosol data assimilation for each experiment condition measured by MODE. All the scores show a 3-month mean from 1 March to 31 May 2007.

Experiment	Centroid distance (0 best; ∞ worst)	Area ratio (1 best; 0 worst)	75th Percentile intensity ratio (1 best; 0 worst)
Free model run (FmR)	2.15	0.49	0.80
Exp-Std	1.45	0.76	0.85
Exp-Ens128	1.46	0.77	0.87
Exp-Ens64	1.44	0.78	0.86
Exp-Ens16	1.47	0.77	0.87
Exp-Ens8	1.52	0.77	0.86
Exp-Inf05	1.43	0.78	0.87
Exp-Inf10	1.48	0.76	0.87
Exp-Inf40	1.46	0.76	0.86
Exp-Lcl1000	1.49	0.78	0.86
Exp-2err	1.46	0.77	0.85
Exp-5err	1.48	0.77	0.86
Exp-Sky	1.42	0.77	0.86
Exp-Cld01	1.53	0.77	0.87
Exp-Cld005	1.49	0.76	0.86
Exp-Hth	1.43	0.78	0.87
Exp-4sat	1.47	0.76	0.87

Table 8. Performance of the dust aerosol data assimilation for each experiment condition measured by MODE. All the scores show a 3-month mean from 1 March to 31 May 2007.

Experiment	Centroid distance (0 best; ∞ worst)	Area ratio (1 best; 0 worst)	75th Percentile intensity ratio (1 best; 0 worst)
Free model run (FmR)	2.59	0.51	0.83
Exp-Std	1.14	0.72	0.85
Exp-Ens128	1.37	0.67	0.86
Exp-Ens64	1.22	0.72	0.86
Exp-Ens16	1.29	0.67	0.83
Exp-Ens8	1.46	0.63	0.83
Exp-Inf05	1.33	0.72	0.86
Exp-Inf10	1.24	0.70	0.83
Exp-Inf40	1.24	0.67	0.84
Exp-Lcl1000	1.35	0.67	0.85
Exp-2err	1.06	0.72	0.86
Exp-5err	1.43	0.53	0.77
Exp-Sky	1.07	0.72	0.85
Exp-Cld01	1.11	0.71	0.85
Exp-Cld005	1.30	0.70	0.85
Exp-Hth	1.86	0.57	0.85
Exp-4sat	1.25	0.65	0.82
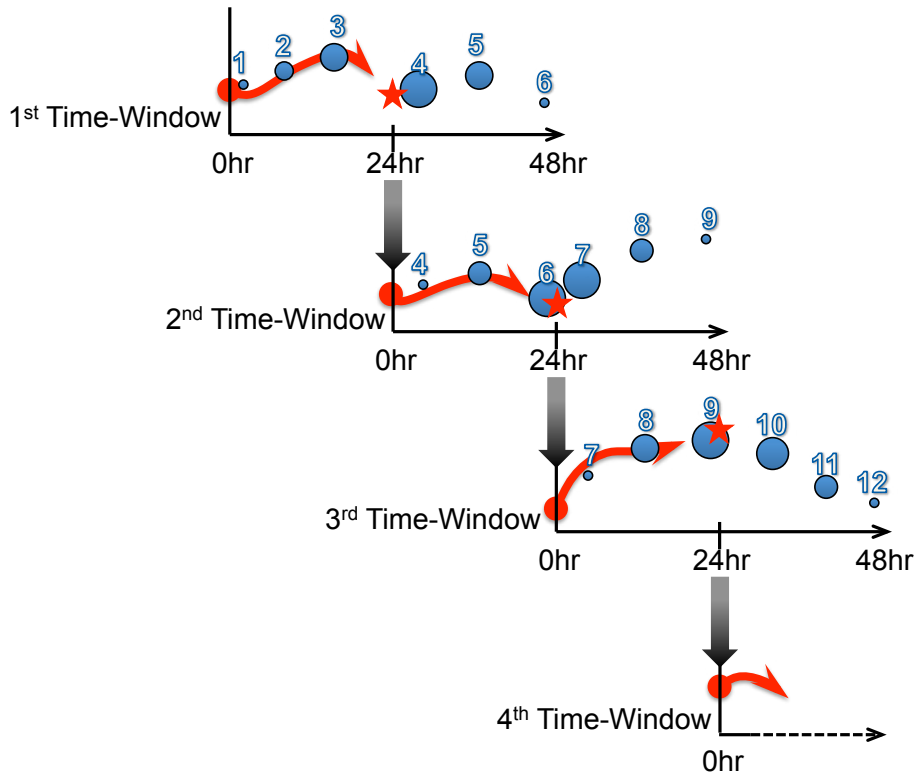
Fig. 1. The schematic diagram of the 4D-LETKF data assimilation scheme. In this case, each time window is 48 h long. The analysis is obtained at the intermediate time of this assimilation time window at 24-h intervals. Red stars indicate the analysis. Red arrows illustrate a temporal transition of the state. Blue circles indicate observations, and the size of each blue circle symbolizes the localization weight that depends on the distance from the analysis grid to the observation grid. Each observation is weighted and used twice. The same observation has the same number in this illustration.

Title Page

Abstract | Introduction

Conclusions | References

Tables | Figures

◄ | ►

◄ | ►

Back | Close

Full Screen / Esc

Printer-friendly Version

Interactive Discussion
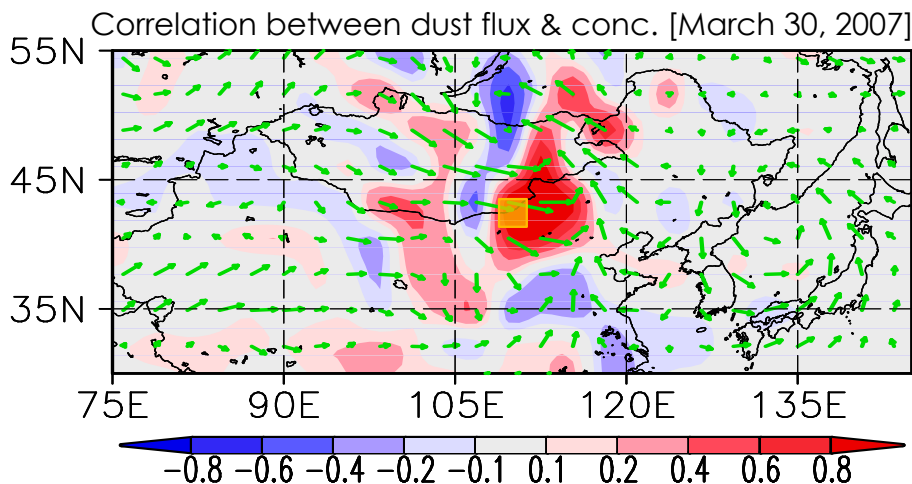
Fig. 2. The correlation between surface dust concentrations and the dust emission within the yellow square area centered at (43° N, 112.5° E). This spatial distribution indicates the response pattern of the dust concentrations to an increase in the dust emission within the yellow square area. This correlation distribution was derived from the 32-member ensemble forecast from 00:00 UTC to 24:00 UTC on 30 March 2007. Green arrows indicate the mean surface winds on this day.

Title Page

Abstract | Introduction

Conclusions | References

Tables | Figures

|◄ | ►|

◄ | ►

Back | Close
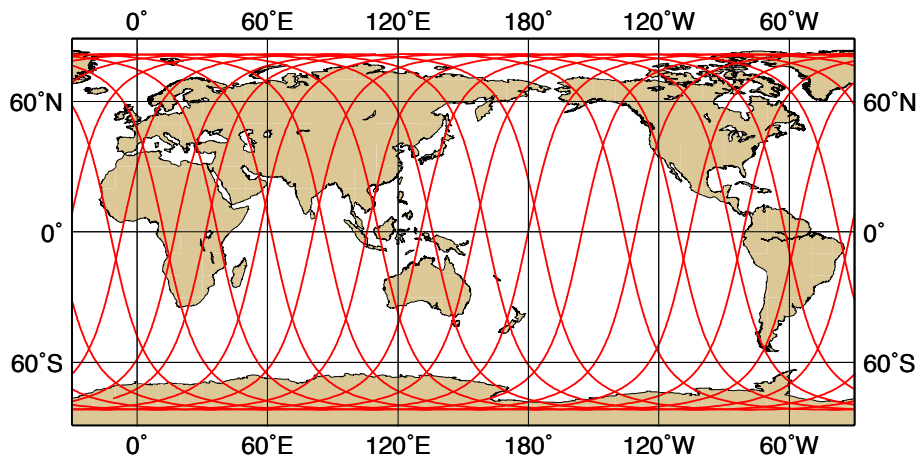
Full Screen / Esc

**Fig. 3.** An example plot of the one-day CALIPSO orbit tracks (1 March 2007).

Full Screen / Esc

Printer-friendly Version

Interactive Discussion
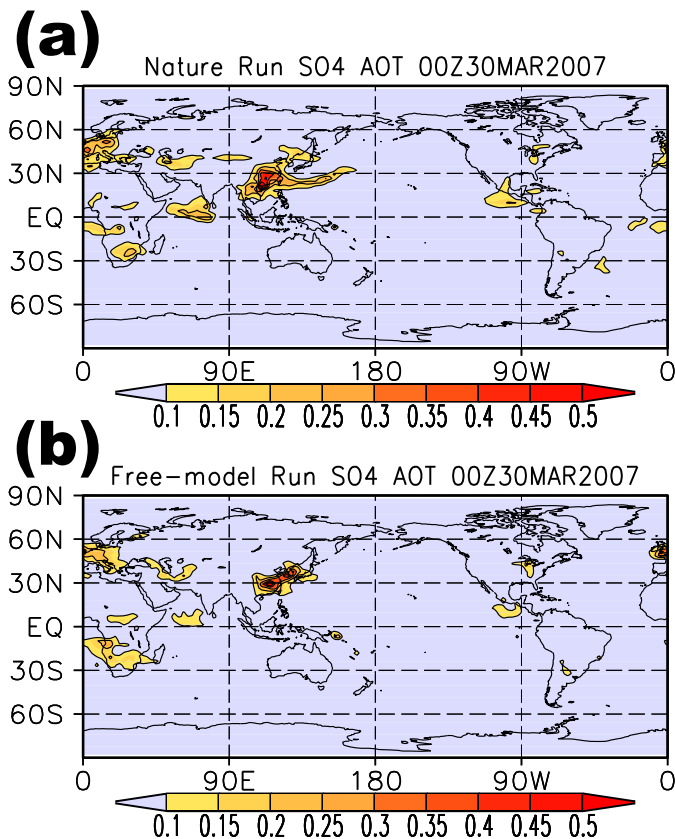
Fig. 4. Snapshots of sulfate aerosol optical thickness (AOT) at 00:00 UTC on 30 March 2007 derived from **(a)** the Nature Run MASINGAR result and **(b)** the default MASINGAR result.
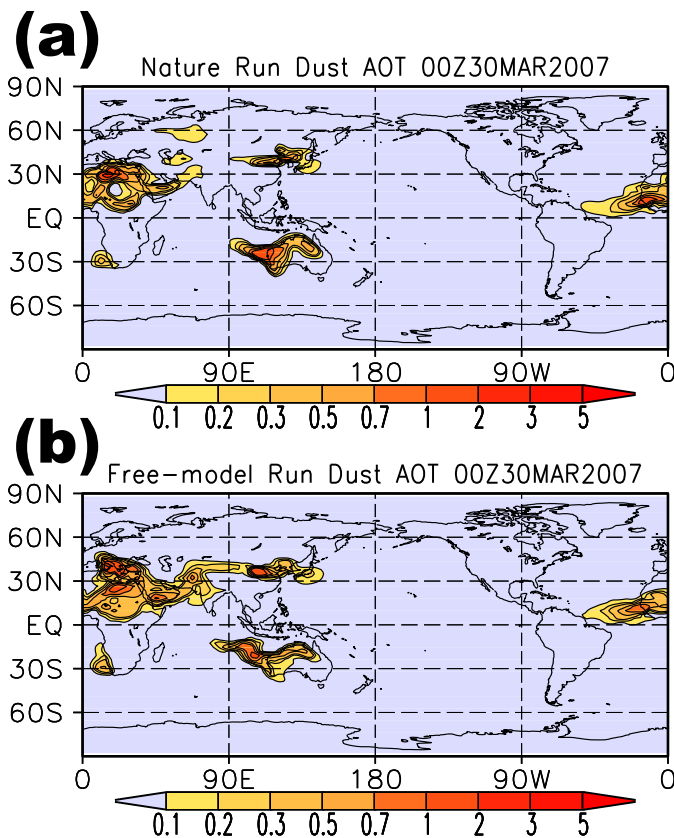
Fig. 5. The same as Fig. 4, but snapshots of dust aerosol optical thickness (AOT).

Cloud Cover Ratio
Sum of 16 Layers below 150hPa 30MAY2007

MTSAT-1R IR 2007-05-30 11:32UTC
Copyright (C) JMA Meteorological Satellite Center (MSC)
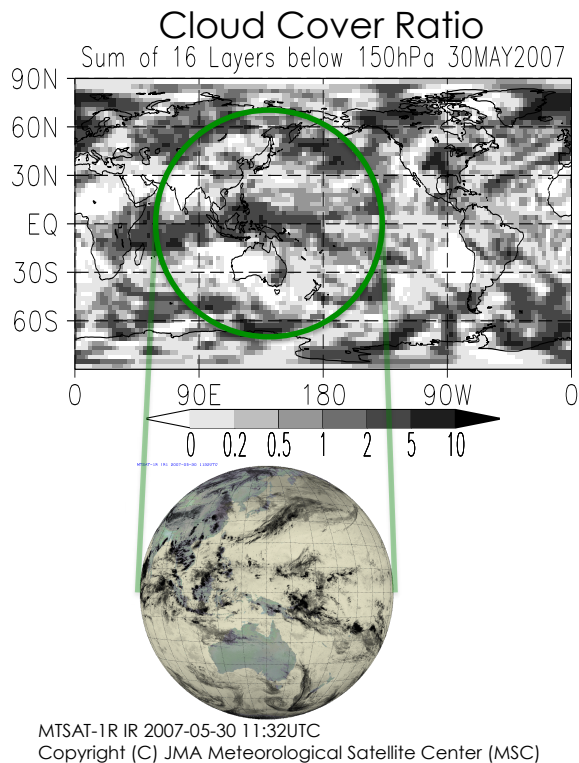
Fig. 6. Upper: the daily-mean cloud cover ratio (CCR) of the Nature Run model result on 30 May 2007, which is the sum (varying from 0 to 16) of the 16-layer CCRs below 150 hPa. Each layer's CCR varies from 0 to 1, in which a zero ratio means a perfectly clear sky. Lower: the real cloud snapshot taken by the infrared channels of the geostationary meteorological satellite MTSAT-1R located at 140° E on the same day. The green circle in the upper panel indicates the approximate location of the snapshot of the lower panel.
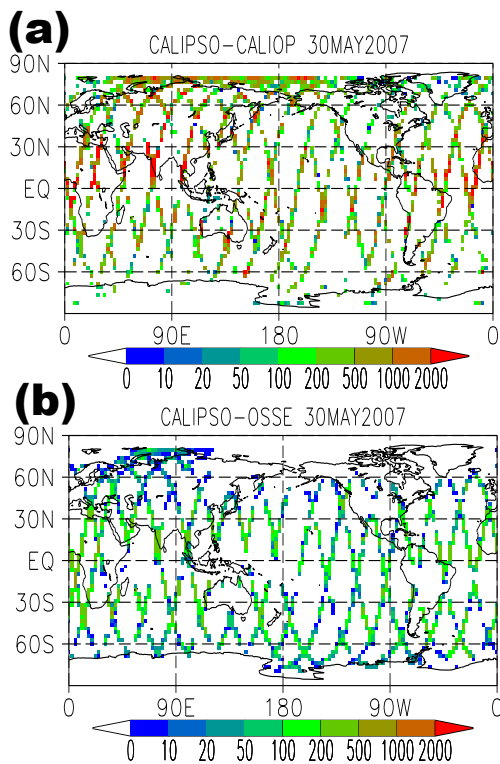
Fig. 7. A distribution of lidar aerosol observations on 30 May 2007 **(a)** derived from the real CALIPSO/CALIOP after screened by the cloud-aerosol discrimination (CAD) scores, and **(b)** derived from the OSSE virtual lidar with the standard settings after screened by the cloud-cover ratio and the aerosol signal threshold. Because the CALIOP vertical resolution is higher than the Nature Run resolution, the total data amount of **(a)** is larger than that of **(b)**.
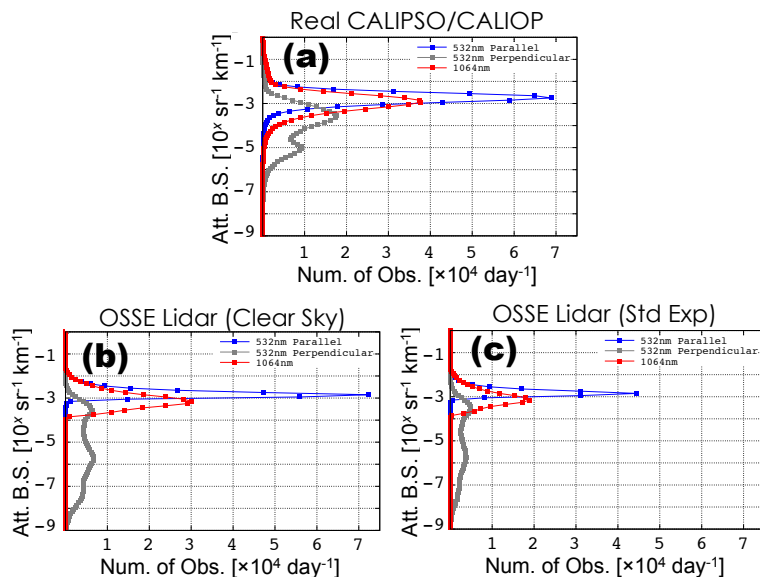
Fig. 8. Frequency distributions of the selected observations to be assimilated in the global troposphere: **(a)** the real CALIPSO/CALIOP observations (Sekiyama et al., 2010), **(b)** the OSSE simulated observations with the perfectly clear sky condition, **(c)** the OSSE simulated observations with the standard conditions. The aerosol signal threshold was set to a $2 \times 10^{-5}\,\mathrm{m}^{-1}$ extinction coefficient at 532 nm for **(b)** and **(c)**. These observations were previously screened by the cloud cover ratio and the aerosol signal threshold but not yet averaged to the model resolution. Thus, the total observation number of **(a)** tends to be larger than that of **(b)** or **(c)**. Blue line and squares indicate 532 nm parallel attenuated backscattering coefficients; red line and squares indicate 532 nm perpendicular attenuated backscattering coefficients; gray line and squares indicate 1064 nm total attenuated backscattering coefficients. The X-axis shows the number of observations. The Y-axis shows the intensity of attenuated backscatter, and is expressed logarithmically.

Title Page

Abstract | Introduction

Conclusions | References

Tables | Figures

◀ | ▶

◀ | ▶

Back | Close

Full Screen / Esc

Printer-friendly Version

Interactive Discussion
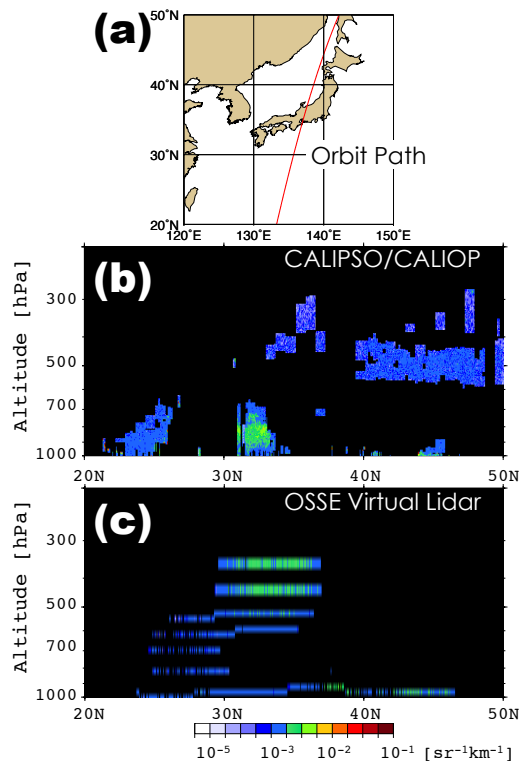
Fig. 9. Cross sections of lidar observations (total attenuated backscattering coefficients at 532 nm) at approximately 17:00 UTC on 27 May 2007 over East Asia along the orbit path shown in **(a)**, **(b)** derived from the real CALIPSO/CALIOP data, and **(c)** derived from the Nature Run. The simulated observations **(c)** have vertically discrete layers depending on the model resolution, distributing them into strips. The real CALIOP observations **(b)** are not yet averaged to either the CAD score resolution or the model resolution.
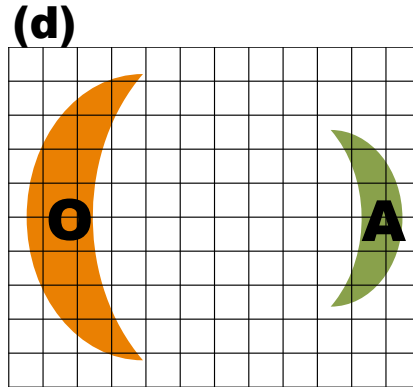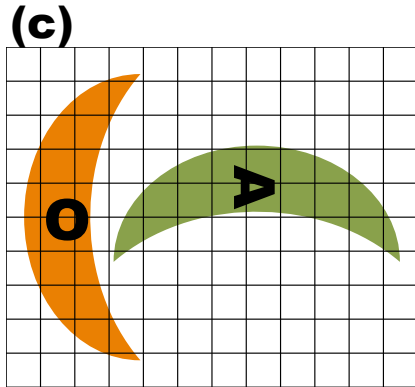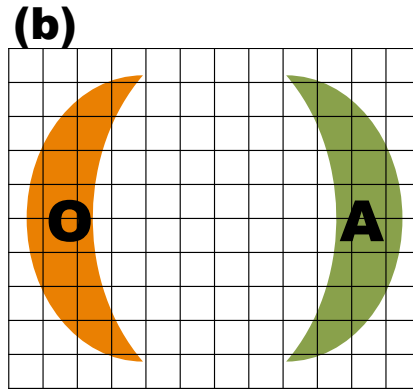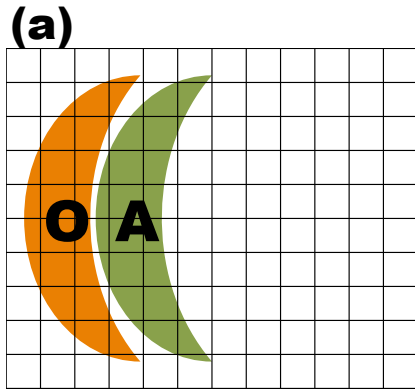
Fig. 10. A schematic example of various observation and analysis combinations. **(a–c)** These all yield the same RMSE, whereas **(d)** has the best RMSE. However, **(a)** would probably be evaluated as the best subjectively.
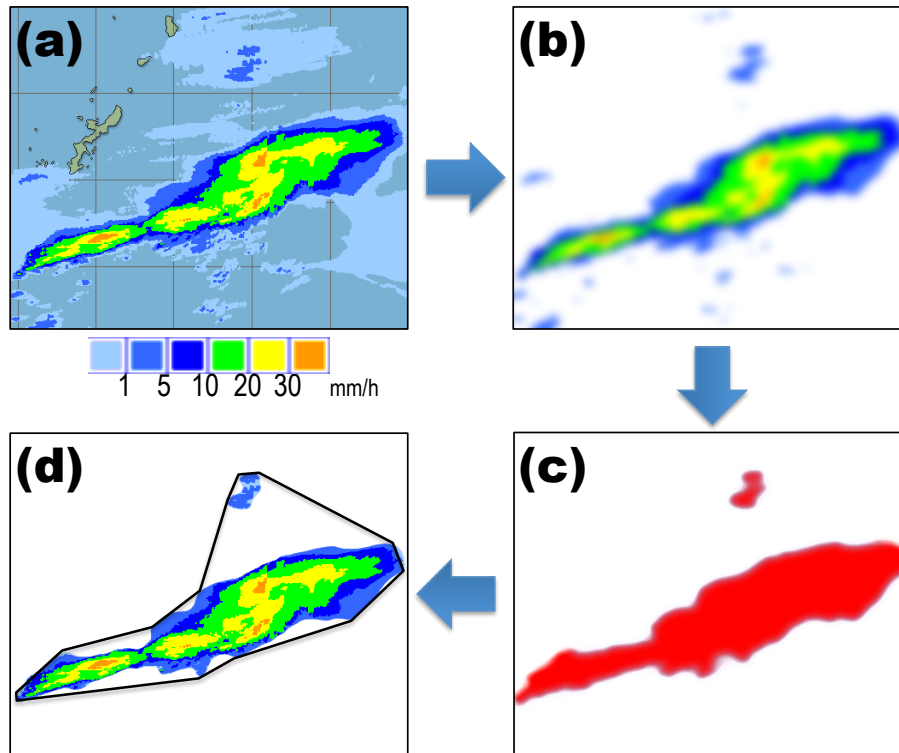
Fig. 11. Example of application of the object-identification approach used in MODE, illustrated by precipitation distribution. **(a)** Original precipitation distribution, **(b)** convolved distribution after the smoothing operation has been applied, **(c)** masked distribution following application of the intensity threshold, and **(d)** filtered distribution showing the precipitation intensities inside the identified objects.
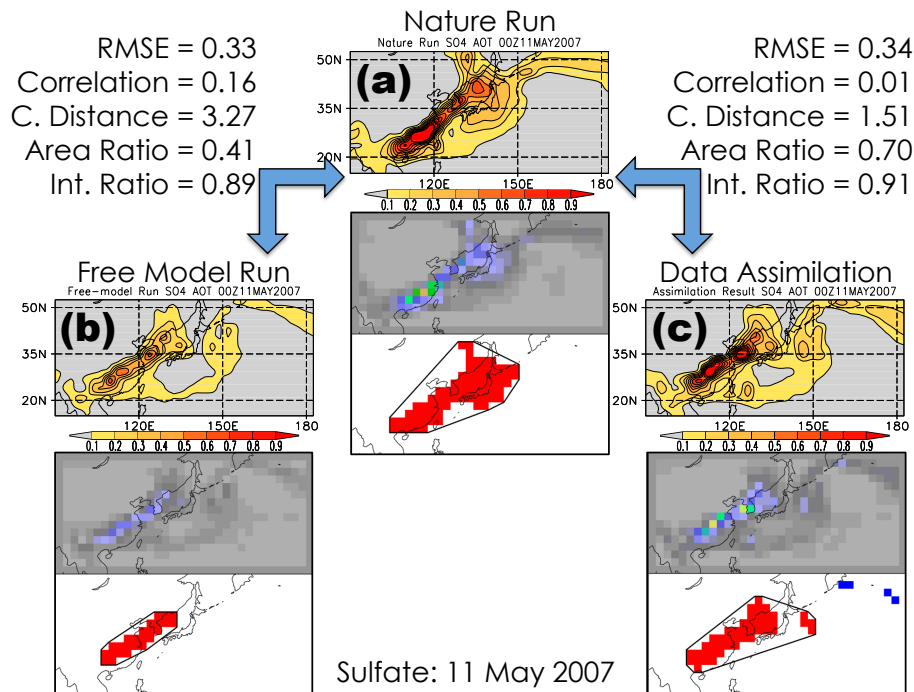
Fig. 12. The comparison of sulfate AOT distributions and performance scores at 00:00 UTC on 11 May 2007: **(a)** the Nature Run, **(b)** the free model run without data assimilation, and **(c)** the data assimilation result with the standard condition. In **(a)**, **(b)**, and **(c)**, the upper panels show the raw data (corresponding to Fig. 11a), the middle panels show the convolved data (corresponding to Fig. 11b), and the lower panels show the masked distributions (corresponding to Fig. 11c). The listed performance scores are RMSE, normal correlation, the distance between two object centroids in grid units, ratio of the areas of two objects, and ratio of the 75th percentile intensity of the two objects.
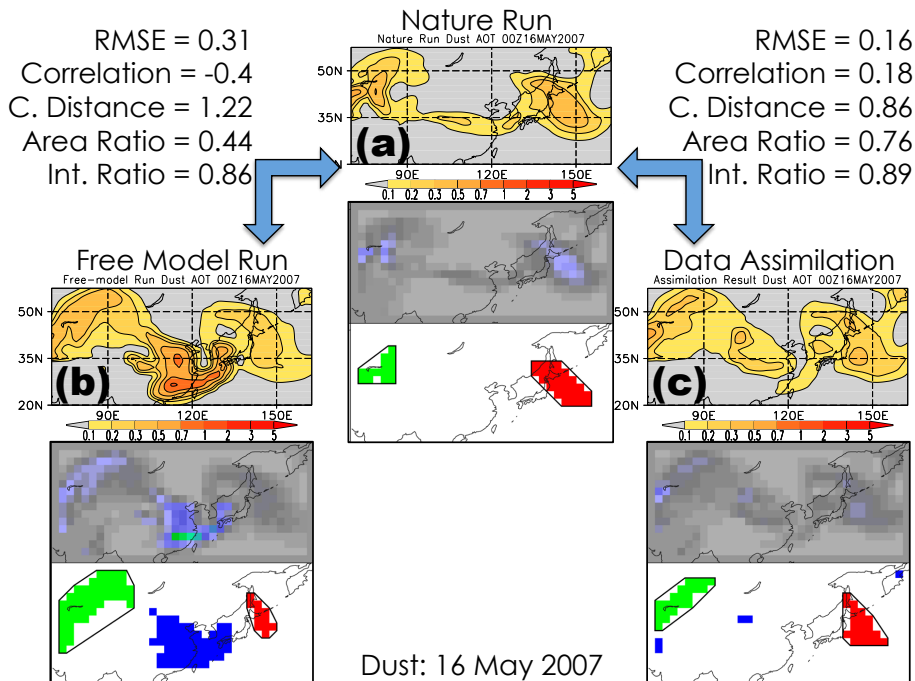
Fig. 13. The same as Fig. 12, but the comparison of dust AOT at 00:00 UTC on 16 May 2007.
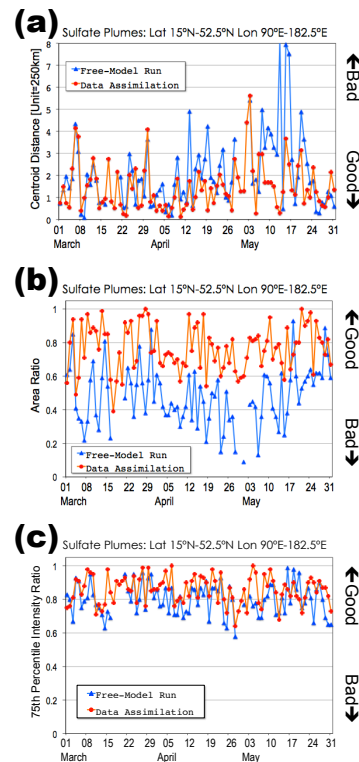
Fig. 14. Time series of **(a)** the two-object centroid distance (grid unit ≈ 280 km), **(b)** the two-object area ratio, and **(c)** the two-object 75th-percentile intensity ratio of sulfate aerosol plumes. Blue triangles indicate the performance of the free model run without data assimilation. Red circles indicate the performance of the data assimilation with the standard condition. The analyzed region was limited in East Asia and the Northwest Pacific from 15° N to 52.5° N in latitude and from 90° E to 182.5° E in longitude. If two or more plumes existed in the region in a day, their distances or ratios were averaged.

Fig. 15. Time series of **(a)** the two-object centroid distance (grid unit ≈ 280 km), **(b)** the two-object area ratio, and **(c)** the two-object 75th-percentile intensity ratio of dust aerosol plumes. Blue triangles indicate the performance of the free model run without data assimilation. Red circles indicate the performance of the data assimilation with the standard condition. The analyzed region was limited in East Asia (mainly China, Mongolia, Korea, and Japan) from 20° N to 57.5° N in latitude and from 70° E to 162.5° E in longitude. If two or more plumes existed in the region in a day, their distances or ratios were averaged.

Title Page

Abstract | Introduction

Conclusions | References

Tables | Figures

|◀ | ▶|

◀ | ▶

Back | Close

Full Screen / Esc

Printer-friendly Version

Interactive Discussion
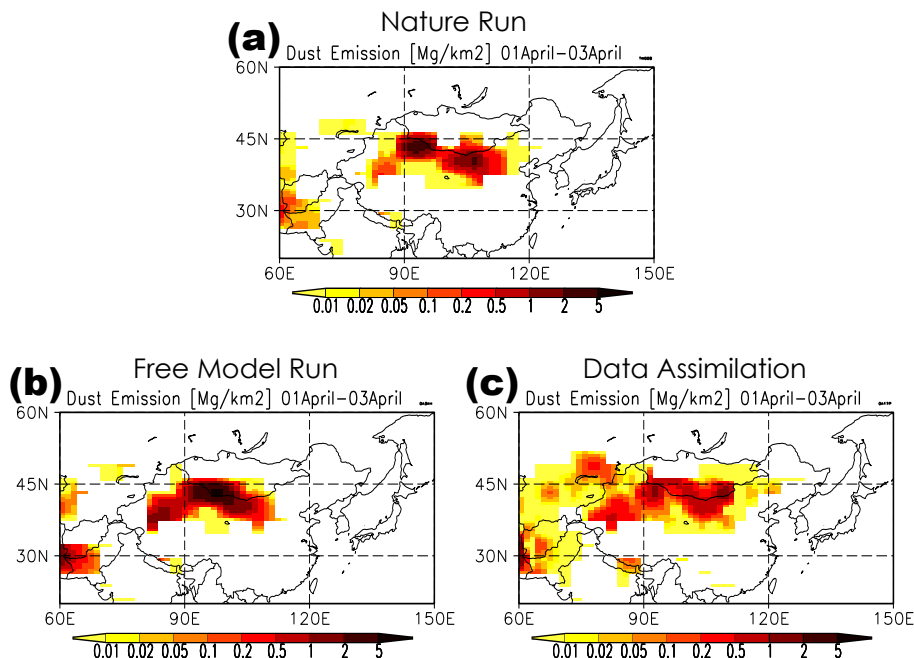
Fig. 16. Dust emission during a dust event from 1 April to 3 April 2007 of **(a)** the Nature Run, **(b)** the free model run without data assimilation, and **(c)** the data assimilation result with the standard condition. The dust weights of six size bins from 0.200 μm to 3.17 μm in diameter were accumulated during the dust event period.
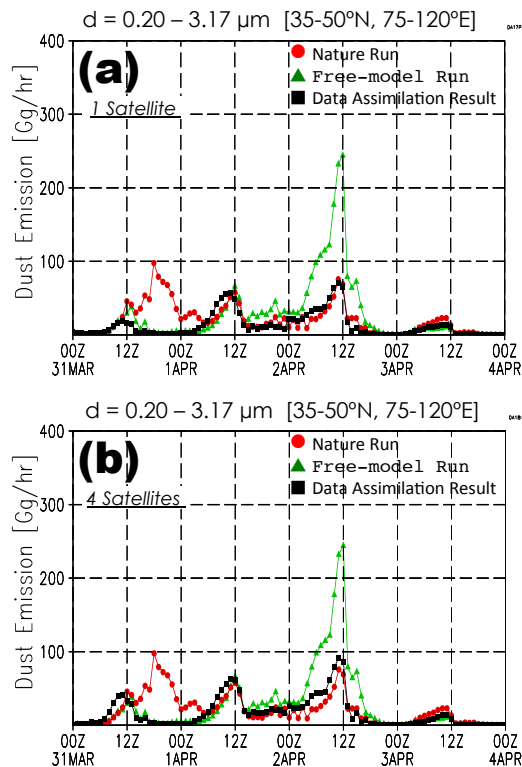
Fig. 17. Time series of the dust emission flux totaled in the Asian Dust source region (mainly China and Mongolia) in early April 2007. The dust weights of six size bins from 0.200 μm to 3.17 μm in diameter were accumulated. Red circles indicate the Nature Run. Green triangles indicate the free model run result without data assimilation. Black squares indicate the data assimilation result with the standard condition. Only one satellite was used for the OSSE in **(a)**, and four satellites were used in **(b)**.
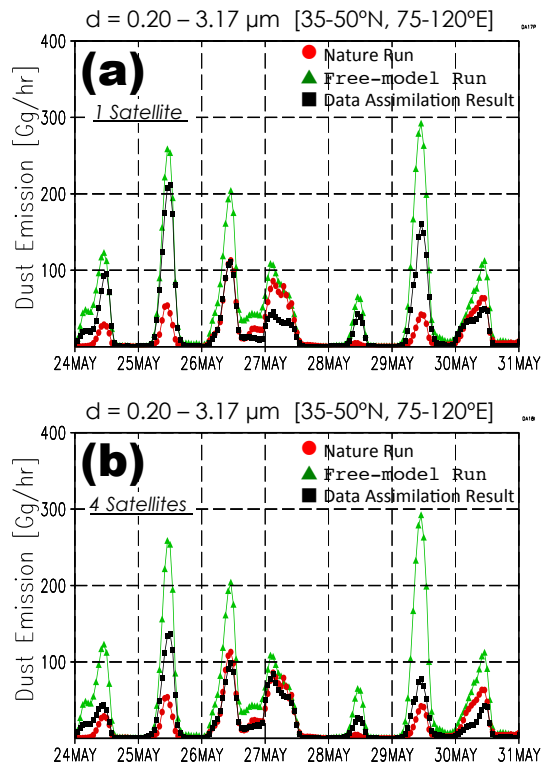
Fig. 18. The same as Fig. 17, but in late May 2007.